Highlights

- Mn_2O_3@Mn_5O_8 shows better catalytic performance than other S(IV) activators
- S(IV) is activated by Mn_2O_3@Mn_5O_2, generating $SO_3^{\bullet-}$, $SO_5^{\bullet-}$, $SO_4^{\bullet-}$, and $^{\bullet}OH$ radicals
- Experiments show phenol is mainly removed by $^{\bullet}OH$, and partially by $SO_4^{\bullet-}$ and $SO_5^{\bullet-}$
- At an initial solution pH of 3.0–7.0, stable degradation of phenol is achieved
- Low toxicity and high S(IV) activation ability of Mn_2O_3@Mn_5O_2 affords a green method

Graphical Abstract

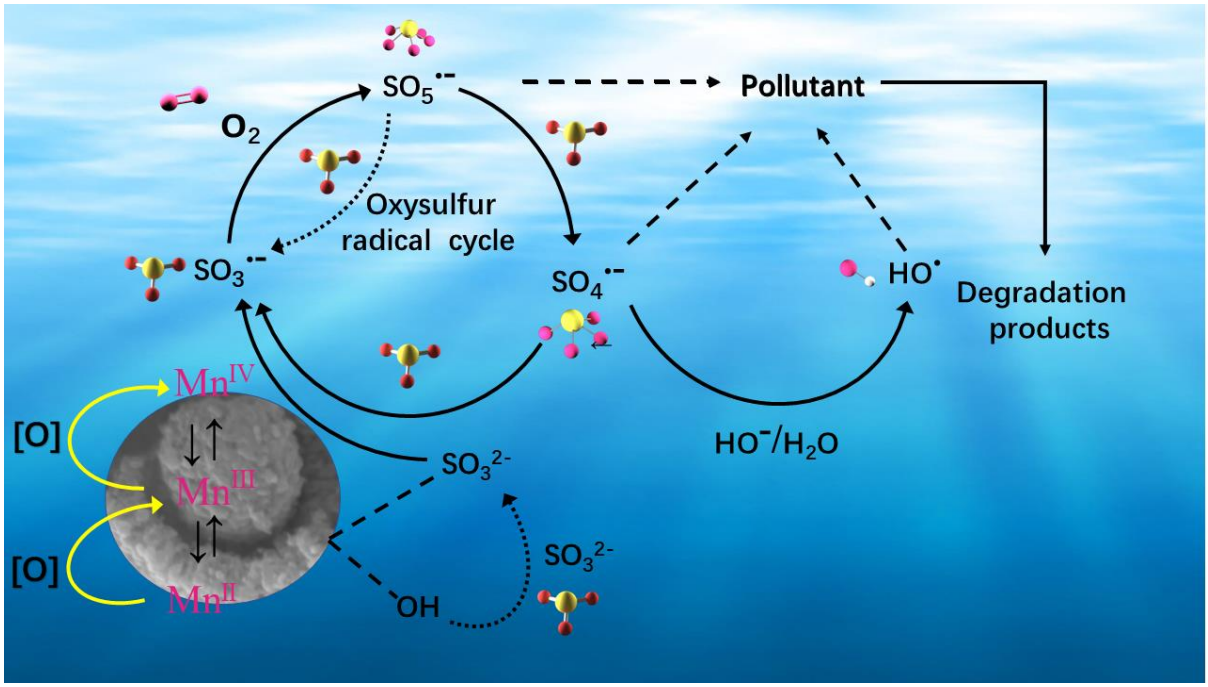

A possible overall sulfite activation mechanism on Mn_2O_3@Mn_5O_8 catalyst for organic contaminant degradation.

$Mn_2O_3@Mn_5O_8$ as an efficient catalyst for the degradation of organic contaminants in aqueous media through sulfite activation

Aimal Khan [a,b], Xianjie Feng [a], Chuankun Yin [c], Habib Ullah [d], Asif Ali Tahir [d], Bowen Li [a], Weiming Wang [a], Xiaoxia Li [a,b,*], Aihua Xu [a,b,*]

[a] School of Chemistry and Chemical Engineering, Wuhan Textile University, Wuhan 430200, China.

[b] Hubei Key Laboratory of Biomass Fibers & Eco-Dyeing & Finishing, Wuhan Textile University, Wuhan 430200, China

[c] School of Environmental Engineering, Wuhan Textile University, Wuhan 430200, PR China.

[d] Environment and Sustainability Institute, University of Exeter, Penryn Campus, Penryn, Cornwall TR10 9FE, United Kingdom

***Corresponding author:** E-mail: xahspinel@sina.com (Aihua Xu), lixxwh@163.com (Xiaoxia Li)

Abstract

Less-toxic, cost-effective, stable, and highly efficient catalysts for sodium sulfite (S(IV)) activation are required to degrade organic pollutants from wastewater. Herein, we report the facile thermal synthesis of Mn_2O_3@Mn_5O_8 that activates S(IV) more efficiently than other Mn and transition-metal oxides. Mn_2O_3@Mn_5O_8 exhibits good performance and long-term stability for eliminating various contaminants from aqueous media, including phenol, bisphenol A, nitrobenzene, 2,4-dichlorophenol, and acetaminophen. Its high performance is attributed to its multivalency, unique architecture, surface hydroxyl groups (–OH), and high surface area. X-ray diffractometry and high-resolution transmission electron microscopy revealed that Mn_2O_3@Mn_5O_8 comprises well-combined cubic Mn_2O_3 and monoclinic Mn_5O_8 crystalline structures, whereas electron paramagnetic resonance spectroscopy and scavenging tests showed that $SO_5^{\bullet-}$, $SO_4^{\bullet-}$, and $^{\bullet}OH$ radicals are generated during S(IV) activation, with $SO_3^{\bullet-}$ as a precursor. The mixed-valence state provides effective and favorable electron transfer via Mn redox cycling (Mn(II)↔ Mn(III) ↔ Mn(IV)), improving the S(IV) activation performance and catalytic activity. Mn_2O_3@Mn_5O_8/S(IV) system shows stable performance in the 3.0–7.0 pH range. Density functional theory calculations confirmed the higher catalytic activity as indicated by high –OH adsorption energy and significant inter-charge transformation. This study provides new insights and strategies for the activation of S(IV) using less-toxic metal oxides as catalysts and broadens the scope of heterogeneous Mn-based catalysts and S(IV) chemistry in real-world applications, particularly for the treatment of wastewater.

Keywords: Transition-metal oxide; Sulfite activation; Advanced oxidation; Organic pollutant; Reactive oxygen species

1. Introduction

Over the past few decades, contaminated wastewater has been released into the environment from various sources, such as industry, hospitals, and daily-life activities, negatively impacting the ecosystem and human health [1,2]. For example, phenol and chlorinated phenol compounds have been reported as priority contaminants for elimination owing to their low biodegradability and high toxicity [3]. However, conventional treatments are inadequate for the elimination of such organic pollutants, thus exhibiting a sluggish removal performance. Thus, the development of environmental-friendly, cost-effective, and highly efficient methods is essential for the elimination of organic pollutants from wastewater matrices.

Advanced oxidation processes (AOPs) are a promising option for wastewater treatment because they can be used to degrade refractory organic pollutants through reactions with highly active radicals. In this regard, persulfate has been used to combat organic contaminants through production of $SO_4^{\bullet-}$ [4,5]. However, due to several limitations, such as high cost, inherent toxicity, and residue retention, the use of persulfate systems may cause secondary environmental pollution [6–8]. Novel sodium sulfite (S(IV))-based AOPs have drawn extensive attention owing to their low cost and environmental-friendly nature. Furthermore, the stability of S(IV) is considerably higher than that of persulfate [6,9]. Moreover, S(IV) is already present in many industrial operations; in addition to being a common reducing agent, it is produced during exhaust gas desulfurization and is present in industrial wastewater as a waste product (pollutant) [10–12]. It can be converted into radicals by metal-based catalysis for the degradation of organic pollutants. For instance, the radicals produced by a Fe(VI)–S(IV) system can degrade phenol and other organic pollutants [13]. In addition, a Mn(VII)–S(IV) system can efficiently eliminate 71% of arsanilic acid [10]. Various transition-metal oxides, including Cr(VI) [14], Fe(II/III) [15,16], and

Ni(II) [6], can be used to activate S(IV) and, thus, produce radicals for the degradation of organic compounds.

In the past few years, Co used as a heterogeneous catalyst and its composites with S(IV) have been analyzed for contaminant degradation owing to their efficient generation of radicals [9,11,12]. Nevertheless, the application of Co-based catalysts for S(IV) or persulfate activation leads to problems related to toxicity [9,17]. As previously reported by our group, Co-based heterogeneous catalysts exhibit excellent catalytic activities for phenol degradation; however, the leaching of Co ions cannot be completely controlled [18]. Fe-based heterogeneous catalysts have also been considered; however, they demonstrate sluggish catalytic performance for S(IV) activation for the generation of radicals [9]. Moreover, Fe-based catalysts produce sludge during wastewater treatment; consequently, their application in AOPs is restricted [2]. Therefore, less-toxic, cost-effective, stable, and more efficient catalysts are crucial for S(IV) activation.

Mn oxides exist in high amounts in soil, are competitively priced, and have low environmental biotoxicities. They are present in three main valence states (Mn^{2+}, Mn^{3+}, and Mn^{4+}), facilitating their application in catalysis [19–21]. The corresponding redox cycle is closely related to the transfer of electrons among the Mn species. Both α-Mn_2O_3@α-MnO_2-500 nanocomposite [22] and egg-shaped core/shell α-Mn_2O_3@α-MnO_2 catalyst [23] showed excellent redox properties due to their multivalent states. Furthermore, they showed outstanding catalytic performance for persulfate activation toward radical production. MnO_2, Mn_2O_3, and Mn_3O_4 catalysts have been widely used in persulfate systems for the degradation of organic contaminants. They demonstrate different catalytic performances for persulfate activation to generate reactive oxygen species (ROS) [22,24]. The catalytic performance of Mn-based catalysts depends on the (multi)valence state, surface area, presence of surface –OH groups, and surface morphology [25,26].

The surface morphology of an Mn oxide can significantly enhance its performance. For example, spheres with hollow, yolk/shell, or core/shell nanostructures that contain a yolk, shell, and/or void space are novel and important nanomorphologies [27,28]. As nanoreactors for catalysis, nanomaterials with such morphologies and porous shells exhibit unique advantages. They exhibit a high degradation performance because both the core/yolk and shell surfaces are exposed, with reactive small molecules passing through the porous shell, providing numerous catalytic sites [27–29]. Unfortunately, many such heterogeneous catalysts have limitations such as high cost, complex synthetic procedures, and low chemical stability during wastewater treatment [30]. Thus, the development of less-toxic solid-based catalysts with stable and high performance for S(IV) activation and a facile synthetic procedure is urgently required.

Herein, the catalytic degradation performance of Mn_2O_3@Mn_5O_8, α-MnO_2, Mn_2O_3, Mn_3O_4, Mn_5O_8, and other transition-metal oxides, such as Co_3O_4, CuO, and Fe_2O_3, toward phenol degradation were extensively examined in the S(IV) system. This study aims to (i) synthesize an efficient catalyst by a facile route, evaluate the catalytic efficiencies of transition-metal oxides, and consequently develop an efficient heterogeneous catalyst for the S(IV) system; (ii) test the broad spectrum of Mn_2O_3@Mn_5O_8/S(IV) systems for the degradation of various organic pollutants; (iii) explore the influence of radical species on the catalytic degradation performance of Mn_2O_3@Mn_5O_8; and (iv) investigate the catalytic performance and cyclability of Mn_2O_3@Mn_5O_8 at different pH. To the best of our knowledge, this is the first study on the use of monometallic oxides as heterogeneous catalysts with significant potential for the degradation of organic pollutants via S(IV) activation.

2. Materials and methods

2.1. Chemicals

Manganese carbonate (≥99.0%), anhydrous sodium sulfite (97.0%), sodium nitrite (99.0%), potassium permanganate (99.5%), maleic acid (≥99.0%), sodium hydroxide (≥96.0%), sulfuric acid (95.0–98.0%), sodium sulfate (≥99.0%), humic acid (HA) (≥90%), ethanol (≥97.7%), tert-butyl alcohol (≥99.0%), phenol (99.0%), 2,4-dichlorophenol (99.0%), bisphenol A (99.0%), acetaminophen (98%), aniline (≥99.0%), and 5,5-dimethyl-1-pyrroline-*N*-oxide (97.0%) were purchased from Aladdin industrial corporation and Sinopharm Chemical Reagent Co., Ltd., China. Nitrobenzene (99.0%) was purchased from Shanghai Lingfeng Chemical Reagent Co., Ltd.

2.2. Synthesis of transition-metal oxide catalysts

2.2.1. Synthesis of Mn_2O_3@Mn_5O_8, Mn_2O_3, and Mn_3O_4

Commercial $MnCO_3$ was calcined at 500, 700, and 900 °C (heating rate: 3 °C min^{-1}) for 2 h to obtain Mn_2O_3@Mn_5O_8, Mn_2O_3, and Mn_3O_4, respectively [31].

2.2.2. Synthesis of Mn_5O_8

To prepare Mn_5O_8, a γ-MnOOH precursor was first synthesized by a hydrothermal method as follows: $KMnO_4$ (0.79 g) was added to water (47 mL) and ethanol (EtOH; 3 mL) in a beaker, with the total volume maintained at 50 mL. The beaker was then transferred to a steel autoclave and sealed. Then, it was held at 140 °C for 24 h. The obtained product was separated by filtration and repeatedly washed with water. Finally, it was dried overnight at 80 °C in an oven. The γ-MnOOH precursor was then calcined at 400 °C (heating rate: 1 °C min^{-1}) for 2 h under nitrogen flow to produce Mn_3O_4 that was subsequently calcined at 410 °C (heating rate: 4 °C min^{-1}) for 2 h in air to obtain Mn_5O_8 [32].

2.3. Catalyst characterization

The various transition metal-based catalysts were characterized by several analytical techniques. The crystallinities and crystal structures of the catalysts were determined by X-ray diffraction (XRD; B.V. Empyrean, PANalytical) using radiation with a wavelength (λ) of 1.5405 Å. Scanning electron microscopy (SEM; FEI Nova Nano) and transmission electron microscopy (TEM; Tecnai G20 American) were used to investigate the surface morphologies of the catalysts. Brunauer–Emmett–Teller (BET) analysis was performed to determine the surface areas of the various catalysts. Compositions and valence states of the catalysts were determined by X-ray photoelectron spectroscopy (XPS; GENESIS, EDAX, USA).

2.4. Experimental procedures

2.4.1. Degradation experiments of organic compounds

Degradation experiments were initiated by placing a 50 μM organic contaminant solution (20 mL) in a conical flask and adding a catalyst (0.004 g) and 0.7 mM S(IV) at 30 °C. The temperature of the reaction solution was adjusted using a water bath, and magnetic stirring was performed at ≥200 rpm. Every 30 min, 0.5 mL samples were withdrawn from the reaction solution, and the amounts of organic pollutants they contained were evaluated. Ethanol (EtOH) and tert-butyl alcohol (TBA) were utilized for scavenging experiments. Other parameters such as the pH, content of anions (Cl^-, SO_4^{2-}, NO_3^-, and CO_3^{2-}), and humic acid (HA) addition were also studied. Furthermore, cycling tests were conducted to investigate the cyclability of Mn_2O_3@Mn_5O_8. At the end of each cycle, the catalyst was removed from the solution through the filtration process, repeatedly washed with water, held at 100 °C in an oven for 12 h, and then used in the next run under similar experimental conditions.

2.4.2. Sample analysis

Every 30 min, the reaction solution (0.5 mL) was passed through a syringe filter (0.45 μm), and phenol concentration was analyzed by high-performance liquid chromatography (HPLC) (Elite 3100, China) using a C18-type column (4.6 × 75 mm, 3.5 μm). The following mobile phases at λ = 270 nm were used for the various contaminants: water and methanol (40:60, v/v) for phenol; water and acetonitrile (40:60, v/v) for bisphenol A (BPA); and water and acetonitrile (50:50, v/v) for nitrobenzene (NB). For acetaminophen (ACE), water and acetonitrile (85:15, v/v) were used as the mobile phase at λ = 254 nm. For 2,4-dichlorophenol (DCP), a mixture of water and acetonitrile (30:70, v/v) was employed as the mobile phase at λ = 210 nm. For all of the tested mobile phases, the flow rate was 1 mL min^{-1}. Total organic carbon (TOC) measurements were conducted to examine the TOC contents of the samples. Initially, 2 mL was withdrawn from the reaction solution, added to a $NaNO_2$ solution (0.3 M, 2 mL) for quenching, and then its TOC was verified [33]. For the curve fitting of the phenol elimination rate in the S(IV) system, a pseudo-first-order equation (equation (1)) was used [34,35]:

$$\ln\left(\frac{C_t}{C_0}\right) = -k_1 t, \quad (1)$$

where C_0 and C_t represent the phenol concentration before the reaction and at reaction time t, respectively, and k_1 is a rate constant.

2.5. Detection of radicals

Electron paramagnetic resonance (EPR) spectroscopy was performed to detect the radicals present in the reaction solution. A spin-trapping reagent 5,5-dimethyl-1-pyrroline-*N*-oxide (DMPO) was introduced to the reaction solution, and then the sample was examined using an EPR spectrometer. The experiments were performed under the following conditions: temperature = 30 °C; power =

10–30 mW; sweep width = 100 G; modulation frequency = 100 GHz; and microwave frequency = 9.90 GHz.

2.6. Computational methodology

Density functional theory (DFT) simulations were performed on Quantum-ATK [36] and the results were analyzed using VESTA and Virtual NanoLab Version 2019.3 software. To validate and confirm the efficiencies of our experimentally observed catalysts, DFT calculations were performed to investigate the effect of oxygen vacancies (O_v) on the interaction between –OH and Mn_2O_3, Mn_5O_8, and Mn_2O_3@Mn_5O_8. The detailed procedure is provided in Text S2.

3. Results and discussion

3.1. Characterization of Mn_2O_3@Mn_5O_8 and other transition-metal oxides

The XRD patterns of α-MnO_2, Mn_3O_4, MnO, Co_3O_4, CuO, and Fe_2O_3 are shown in Fig. S1, and are in accordance with those reported previously [37,38]. In the XRD pattern of Mn_5O_8, the main diffraction peaks were obtained at the 2θ angles of 18.08°, 21.62°, 24.68°, 28.65°, 31.78°, 36.24°, 36.94°, 38.84°, 39.24°, 43.43°, 48.30°, 49.59°, 58.58°, and 66.49° (Fig. 1); this indicates that Mn_5O_8 has a characteristic monoclinic structure with the *C*2/*m* space group (PDF # 39-1218) [32]. Furthermore, in the XRD pattern of Mn_2O_3, diffraction peaks were obtained at the 2θ angles of 23.15°, 32.97°, 38.23°, 45.17°, 49.34°, 55.18°, and 65.08° (Fig. 1), implying that Mn_2O_3 has a cubic structure with the *Ia*3 space group (PDF # 41-1442) [39]. The XRD pattern of Mn_2O_3@Mn_5O_8 exhibited well-defined diffraction peaks of the combined Mn_5O_8 and Mn_2O_3 phases (Fig. 1); no peaks of other Mn oxides were detected, suggesting the successful generation of Mn_2O_3@Mn_5O_8. This type of material with multivalent states and combined crystal structures demonstrates efficient catalytic performance [23,40], as discussed herein.

198 Figs. 2 and S2 show the surface structures of the various samples determined by SEM. The α-
199 MnO_2 particles were in the form of nanorods with various lengths (55–202 nm) and widths (31–
200 68 nm) (Fig. S2a and b). Nanorods were also observed for Mn_5O_8, with the lengths of
201 approximately 1–12 μm and widths of 40–470 nm (Figs. 2a–2c).

202 Mn_2O_3@Mn_5O_8, which was formed by calcining $MnCO_3$ at 500 °C, contained spheres and
203 yolk/shell structures, with the former primarily being non-uniform with an average diameter of 1.2
204 μm, as indicated by the histogram shown in Fig. S3 and the SEM results in Figs. 2d–2f, and Fig.
205 S2(c–f). Moreover, the yolk and shell were composed of small particles with the diameters of 28–
206 78 nm and agglomerated particles of different sizes. The broken shell of Mn_2O_3@Mn_5O_8 clearly
207 showed a void space between the yolk and shell that will provide additional active sites that are
208 beneficial for catalysis [27,28] (Figs. 2f and S2(c–f)). To further confirm the morphology of
209 Mn_2O_3@Mn_5O_8, high-resolution transmission electron microscopy (HRTEM) was conducted
210 (Figs. 3a–3b and S4(a and b). The HRTEM images of Mn_2O_3@Mn_5O_8 were in accordance with
211 the SEM results, as shown in Figs. S4(a and b). Moreover, the interplanar spacings on the surfaces
212 of the Mn_2O_3@Mn_5O_8 particles were measured as 0.49 and 0.27 nm, corresponding to the
213 Mn_5O_8(200) and Mn_2O_3(222) planes, respectively (Figs. 3a and 3b). The insets in Figs. 3a and 3b
214 depict the 2D fast Fourier transforms of the Mn_2O_3@Mn_5O_8 particle that are consistent with those
215 of the (200) plane of monoclinic Mn_5O_8 and the (222) plane of cubic α-Mn_2O_3. These results
216 appropriately agree with the abovementioned XRD results (Fig. 1). Thus, the HRTEM results
217 confirmed that Mn_2O_3@Mn_5O_8 consists of spheres and yolk/shell structures and coexisting
218 monoclinic Mn_5O_8 and cubic Mn_2O_3 crystal structures.

219 The Mn_2O_3 and Mn_3O_4 samples formed by calcining $MnCO_3$ at 700 and 900 °C, respectively, were
220 also examined by SEM. Unlike Mn_2O_3@Mn_5O_8, which was formed by calcining $MnCO_3$ at 500

°C, spherical particles were not observed for Mn_2O_3, and only nanoparticles with different shapes and sizes ranging from 45 to 175 nm were formed (Figs. 2g–2i). When the calcining temperature was further increased to 900 °C, the resultant Mn_3O_4 particles had various shapes and significantly larger sizes (0.65–1.30 μm) (Fig. S2(h–i)) than those of Mn_2O_3@Mn_5O_8. This observation indicated that the particle size of the material increased with increasing calcination temperature. Overall, the abovementioned unique architecture is crucial for achieving a high content of active sites that enhances S(IV) activation and chemical reactions toward the desired target.

3.2. Oxidation of organic pollutants on catalysts

Under identical conditions, the various metal oxides showed different catalytic performance for the degradation of several organic compounds in the presence of S(IV) (Fig. 4). Phenol did not degrade in the presence of S(IV) (0.7 mM) alone within 180 min at 30 °C (Fig. 4a); this demonstrated that the production of ROS from S(IV) could not occur in the absence of a catalyst. When α-MnO_2, Mn_2O_3, Mn_3O_4, and Mn_5O_8 were separately introduced as catalysts into the S(IV) system, 21%, 41%, 17%, and 30% of phenol, respectively, was degraded within 180 min. Similarly, when Mn_2O_3@Mn_5O_8 was introduced into the S(IV) system, 91% of phenol was degraded (Fig. 4a), implying that Mn_2O_3@Mn_5O_8 had a higher activity for phenol degradation than the other S(IV) activators under similar conditions. Clearly, Mn_2O_3@Mn_5O_8 showed a higher phenol degradation efficiency than heterogeneous α-MnO_2, Mn_2O_3, Mn_3O_4, and Mn_5O_8. The efficient catalytic performance of Mn_2O_3@Mn_5O_8 can be attributed to its multivalent states, unique architecture, surface hydroxyl groups (–OH), and large surface area (these features are similar to those reported previously [27,29,39–41]), leading to the generation of more ROS with Mn_2O_3@Mn_5O_8 than with the other S(IV) activators.

The phenol degradation curves of the different catalysts were fitted by the pseudo-first-order kinetic model (Fig. S5) [25,34]. The k_1 values of all the catalysts are listed in Table 1. Mn_2O_3@Mn_5O_8 showed the highest k_1 value of 0.0167 min^{-1}, whereas Mn_3O_4 showed a k_1 value of 0.0014 min^{-1}. Moreover, Mn_2O_3@Mn_5O_8 showed superior catalytic performance compared to that of the other S(IV) activators, including the transition-metal oxides CuO, Co_3O_4, and Fe_2O_3 (Fig. 4b). A filtered solution of Mn_2O_3@Mn_5O_8 was used for catalytic S(IV) activation (Fig. S6). The results indicated that the catalytic activity did not arise from ions; instead, it originated from Mn_2O_3@Mn_5O_8 itself due to its intrinsic features [42]. We also noticed that other pollutants could be effectively removed by the Mn_2O_3@Mn_5O_8/S(IV) system. For example, 100%, 98%, 82%, and 53% of BPA, ACE, DCP, and NB, respectively, were degraded by the Mn_2O_3@Mn_5O_8/S(IV) system under identical conditions (Fig. 4c). This observation suggests that several organic pollutants can be removed by the Mn_2O_3@Mn_5O_8/S(IV) system, which is significant for wastewater treatment.

3.2.1. Cycling tests and stable performance of Mn_2O_3@Mn_5O_8

For an efficient catalytic system, cyclability and stability are two of the most important qualities. For many heterogeneous catalysts, the catalytic performance decreases upon their repeated use in cycling tests [24,33]. For the present system, four successive cycling tests were conducted to determine the cyclability of Mn_2O_3@Mn_5O_8 for the removal of phenol (Fig. 4d). Within 180 min, phenol elimination decreased slightly by the second cycle, whereas phenol degradation decreased from 91% to 86% and 80% by the third and fourth cycle, respectively, corresponding to excellent cycling performance. These results were also supported by the XRD results, which showed that all the major XRD peaks were retained after the reaction (Fig. S7); this indicates the good stability of the Mn_2O_3@Mn_5O_8 structure. The SEM image of the surface morphology of Mn_2O_3@Mn_5O_8 after

the reaction is shown in Fig. S2g. The surface of the Mn_2O_3@Mn_5O_8 sample subjected to cycling consisted of spherical particles that were also observed for the fresh Mn_2O_3@Mn_5O_8 sample. This demonstrates that during the cycling tests, the surface morphology of the catalyst did not change. To summarize, these findings indicate that Mn_2O_3@Mn_5O_8 exhibits significant stability and reusability for S(IV) activation to degrade phenol.

3.3. Mechanism of S(IV)-based AOPs

3.3.1. Detection of reactive radicals

S(IV) can be activated by metal-based catalysts to generate radicals [9–11]. Herein, to explain the activation mechanism of the Mn_2O_3@Mn_5O_8/S(IV) system, we initially performed quenching experiments using different scavengers to determine the ROS in the reaction solution and those participating in the reaction. Fig. 5a depicts the radical-scavenging effects of EtOH, TBA, and aniline. $SO_4^{\bullet-}$ and $^{\bullet}OH$ radicals are quenched by EtOH because it possesses a high reaction rate constants (k) for both $SO_4^{\bullet-}$ ($k = 1.6 \times 10^7\ M^{-1}\ s^{-1}$) and $^{\bullet}OH$ ($k = 1.9 \times 10^9\ M^{-1}\ s^{-1}$) [6,12]. However, EtOH does not have a strong quenching effect on $SO_5^{\bullet-}$ due to the lower k value ($k < 1 \times 10^3\ M^{-1}\ s^{-1}$) [43]. The removal of phenol decreased from 91% to 62% when 100 mM of EtOH was added to the Mn_2O_3@Mn_5O_8/S(IV) system, and to 37% when 500 mM of EtOH was added. TBA is commonly used as a scavenger for $^{\bullet}OH$ ($k = 6.0 \times 10^8\ M^{-1}\ s^{-1}$) [6,44]. When TBA was introduced into the Mn_2O_3@Mn_5O_8/S(IV) system, the degradation of phenol decreased from 91% to 75% (100 mM TBA) and 49% (500 mM TBA). These results indicate that the Mn_2O_3@Mn_5O_8/S(IV) system generates both $SO_4^{\bullet-}$ and $^{\bullet}OH$ radicals, which is consistent with previous reports that S(IV) produces $SO_4^{\bullet-}$ and $^{\bullet}OH$ in the presence of a catalyst [9,12,44]. Furthermore, because the results of the scavenging experiments with EtOH and TBA were somewhat similar, it is likely that $SO_4^{\bullet-}$ rapidly transferred to $^{\bullet}OH$ in this system.

289 The presence of $^{\bullet}OH$ radicals was further verified by using the selective scavenger CO_3^{2-} (see
290 Section 3.8.3) and the chemical probe NB. NB has a high *k* value for $^{\bullet}OH$ ($k = 3.9 \times 10^9$ M^{-1} s^{-1})
291 and does not directly react with $SO_4^{\bullet-}$ [42,45], making it an appropriate chemical probe for
292 confirming the production of $^{\bullet}OH$. Nearly 53% of NB was removed by the Mn_2O_3@Mn_5O_8/S(IV)
293 system (Fig. 4c), suggesting that $^{\bullet}OH$ radicals are the major species responsible for the elimination
294 of contaminants. However, because phenol degradation still occurred to some extent when a large
295 amount (500 mM) of EtOH or TBA was added, active oxygen species other than $SO_4^{\bullet-}$ and $^{\bullet}OH$
296 must be involved in the degradation of phenol. Therefore, aniline was used as an active scavenger
297 for $SO_5^{\bullet-}$ [43]. With the addition of only 5 mM of aniline, the degradation of phenol decreased
298 from 91% to 10% in the Mn_2O_3@Mn_5O_8/S(IV) system. Notably, this is very similar to the extent
299 of phenol oxidation by Mn_2O_3@Mn_5O_8 alone (9.0%) (Fig. 12b), indicating that $SO_5^{\bullet-}$ played a key
300 role in the degradation of phenol in this system. Because almost no phenol was degraded in the
301 presence of aniline alone, we propose that $SO_5^{\bullet-}$ acts as a precursor for the production of $SO_4^{\bullet-}$.

302 EPR spectroscopy measurements were conducted using DMPO as a spin-trapping agent to further
303 confirm the participation of the $SO_3^{\bullet-}$, $SO_4^{\bullet-}$, and $^{\bullet}OH$ radicals (Figs. 5b and 5c). In the absence of
304 a catalyst, the EPR spectrum did not contain signals corresponding to $SO_3^{\bullet-}$, whereas when
305 Mn_2O_3@Mn_5O_8 was introduced into the S(IV) system, a strong signal was detected for a DMPO–
306 SO_3 adduct after 2 min (Fig. 5b); the EPR spectrum was in agreement with those reported in the
307 literature [44,46]. Furthermore, six lines corresponding to DMPO–SO_4 adducts (Fig. 5b) [46] and
308 four lines corresponding to DMPO–OH adducts (after 30 min) were observed in the EPR spectrum
309 of the Mn_2O_3@Mn_5O_8/S(IV) system (Fig. 5c) [44]. Note that DMPO cannot trap $SO_5^{\bullet-}$ to provide
310 an observable signal, even if $SO_5^{\bullet-}$ is present in the reaction solution. However, $SO_3^{\bullet-}$ is readily
311 oxidized to $SO_5^{\bullet-}$ in the presence of dissolved oxygen (see equation (6); $k = 2.5 \times 10^9$ M^{-1} s^{-1}).

312 The role of $SO_5^{\bullet-}$ was verified by investigating the phenol degradation in a Mn_2O_3@Mn_5O_8/S(IV)–
313 N_2 system, in which $SO_3^{\bullet-}$ cannot oxidize to $SO_5^{\bullet-}$ due to the inert conditions. Negligible phenol
314 degradation occurred, as shown in Fig. S8, demonstrating that $SO_5^{\bullet-}$ contributes to phenol
315 degradation. This also confirms that the oxidation of phenol by $SO_3^{\bullet-}$ is negligible.

316 These results imply that S(IV) is activated in the presence of Mn_2O_3@Mn_5O_8 to generate $SO_3^{\bullet-}$,
317 which then acts as a precursor for the production of $SO_5^{\bullet-}$ and then $SO_4^{\bullet-}$. The $SO_4^{\bullet-}$ radical species
318 react with $^-OH/H_2O$ to generate $^\bullet OH$ radicals, which are the primary components involved in the
319 degradation of phenol along with $SO_5^{\bullet-}$ and $SO_4^{\bullet-}$.

320 **3.4. H_2-TPR analysis**

321 To understand the reduction/oxidation behaviors of the catalysts, the H_2 temperature-programmed
322 reduction (H_2-TPR) profiles of the Mn_2O_3@Mn_5O_8, Mn_2O_3, and Mn_5O_8 catalysts between 50 and
323 800 °C are shown in Fig. 6a. The H_2-TPR profiles contain reduction peaks at 301.5 and 403.6 °C
324 for Mn_2O_3@Mn_5O_8, 385.5 and 463.7 °C for Mn_2O_3, and 290.5 and 409.7 °C for Mn_5O_8. The lower
325 and higher temperature peaks were ascribed to the reduction of each catalyst to Mn_3O_4, and of
326 Mn_3O_4 to MnO, respectively. Indeed, XRD patterns of the reduced samples proved the existence
327 of MnO, as shown in Fig. S9. Notably, the present construct of the Mn_2O_3@Mn_5O_8 structure is of
328 multivalent Mn ions in Mn_5O_8 (compositional formula of Mn_2^{II}, $Mn_3^{IV}O_8$ [47]), along with Mn_2O_3
329 (which contains Mn^{III}). Thus, the H_2-TPR results can be explained by the fact that Mn_5O_8 contains
330 Mn^{IV}, which is reduced at a lower temperature than Mn^{III} [48,49], whereas the second peak of
331 Mn_2O_3@Mn_5O_8 was lower than that of the other two samples. This confirmed that the catalyst
332 underwent a Mn(IV) → Mn(III) → Mn(II) transition, which is favorable for the redox cycle of the
333 Mn species within the catalyst.

3.5. Electrochemical test

The different Mn-based catalysts showed different catalytic performance for the degradation of phenol, as shown in Fig. 4a. To elucidate the differences among the catalysts, it is important to study their redox properties. Efficient catalytic performance is also related to the electrochemical behavior because the catalytic reaction to generate ROS involves the transfer of electrons between the catalyst and S(IV).

To verify the charge transfer behavior and redox mechanism of Mn_2O_3@Mn_5O_8, cyclic voltammetry (CV), linear sweep voltammetry (LSV), and electrochemical impedance spectroscopy (EIS) analyses were conducted on the Mn_2O_3@Mn_5O_8, Mn_2O_3, and Mn_5O_8 electrodes in a mixed solution of Na_2SO_4 (0.1 M) and S(IV) (0.7 mM). Fig. 6b shows clear cathodic and anodic peaks corresponding to the oxidation and reduction of the Mn species, which are typical processes in the catalytic reactions on the surface of Mn-based catalysts [40,50]. In the CV curves, the Mn_2O_3@Mn_5O_8 electrode produced remarkable oxidation and reduction potential peaks that were more intense than those produced by the Mn_2O_3 and Mn_5O_8 electrodes. This indicates that the Mn species is important for S(IV) activation, which facilitates fast electron transfer in Mn_2O_3@Mn_5O_8. The current densities of the Mn_2O_3@Mn_5O_8, Mn_2O_3, and Mn_5O_8 samples were calculated from their LSV curves (Fig. 6c). Mn_2O_3@Mn_5O_8 had a higher current density than that of Mn_2O_3 and Mn_5O_8, indicating that the charge transfer ability was considerably enhanced with the addition of Mn_2O_3@Mn_5O_8 [51]; thus, the electron transfer with S(IV) was enhanced. In the high-frequency region of the EIS Nyquist plot (Fig. 6d), Mn_2O_3@Mn_5O_8 produced a smaller semicircle than Mn_2O_3 and Mn_5O_8, indicating efficient charge transfer within the catalyst. The outstanding conductivity and multivalence of the Mn_2O_3@Mn_5O_8 yolk/shell structure can enhance the electron transfer in the Mn_2O_3@Mn_5O_8/S(IV) system. Thus, Mn_2O_3@Mn_5O_8 promotes

electron transfer for efficient S(IV) activation, which can accelerate the elimination of organic pollutants. Overall, compared to the other catalysts, Mn_2O_3@Mn_5O_8 preserved greater redox potential and provided faster electron circulation, which is beneficial for efficient S(IV) activation.

3.6. Plausible S(IV) activation and radical formation pathways

To explore the roles of the surface activation mechanism and chemical composition of Mn_2O_3@Mn_5O_8 on the activation of S(IV) toward the production of $SO_5^{\bullet-}$, $SO_4^{\bullet-}$, and $^{\bullet}OH$, XPS was performed before and after the reactions of the samples (Figs. 7a–d and S10). Before catalytic oxidation, Mn peaks appeared at 640.7, 642.0, and 643.8 eV after peak fitting in the $2p_{3/2}$ core region, which were ascribed to Mn(II), Mn(III), and Mn(IV), respectively [52]. After the reaction, the proportion of Mn(II) increased from 16.1% to 23.0%, whereas the proportions of Mn(III) and Mn(IV) decreased from 44.4% to 39.8% and 39.5% to 37.2%, respectively (Figs. 7a and 7b). This indicates that the Mn(II) ↔ Mn(III) ↔ Mn(IV) redox cycle occurred among the Mn species present during S(IV) activation. The Mn species in the heterogeneous catalyst served as an electron transfer agent for S(IV) activation [6,9] and thus generated oxysulfur radicals.

Figs. 7c and 7d show the O 1s spectra of Mn_2O_3@Mn_5O_8 before and after the reaction, respectively. In the XPS spectra of O(I), O(II), and O(III), three peaks were observed at 529.7, 531.4, and 533.5 eV, corresponding to lattice O (O^{2-}), –OH groups, and adsorbed H_2O, respectively [40]. After the oxidation of Mn_2O_3@Mn_5O_8, the relative intensities of the O^{2-} and adsorbed H_2O peaks increased from 53.6% to 66.2% and 9.8% to 12.3%, respectively, whereas that of the –OH group peak decreased from 36.6% to 21.5%. This result implies that the O species participated in the catalytic reaction and facilitated S(IV) activation via complexation/bond formation. Furthermore, the –OH groups in the catalyst offered active sites for bond formation with S(IV) [9]. Figs. 7c–7f show that Mn_2O_3@Mn_5O_8 had the highest percentage of –OH groups

on its surface (36.6% vs. 28.7% for Mn_2O_3 and 16.7% for Mn_5O_8). Thus, this catalyst facilitated fast electron transfer among the Mn species (Mn(II) ↔ Mn(III) ↔ Mn(IV)) and provided a large number of active sites (–OH groups) for S(IV) activation.

The plausible mechanism for S(IV) activation by Mn_2O_3@Mn_5O_8 is as follows. Initially, a Mn(II/III/IV)–OH complex was generated due to the physical adsorption of H_2O molecules on the Mn_2O_3@Mn_5O_8 surface [6,9,25]. Subsequently, S(IV) formed a complex/bond with Mn(II/III/IV)–SO_3^- via the –OH groups [6,9], allowing electron transfer between the catalyst and S(IV) in the solution. The Mn(II/III/IV)−SO_3^- bonds were broken by another SO_3^{2-} ion, producing $SO_3^{\bullet-}$ according to equations (2) and (3). The electron transfer between Mn_2O_3@Mn_5O_8 and S(IV) was verified by the corrosion current of 4.8×10^{-9} A in the Tafel curves (Fig. S11). This provides strong evidence for S(IV) activation by electron transfer from Mn_2O_3@Mn_5O_8. The CV curves for the Mn_2O_3@Mn_5O_8/S(IV) system showed two reduction peaks at 0.07 and 1.00 V, corresponding to the reduction of Mn^{IV} to Mn^{III} and Mn^{III} to Mn^{II}, respectively. In contrast, two oxidation peaks were detected at 0.80 and −0.19 V corresponding to the oxidation of Mn^{II} to Mn^{III} and Mn^{III} to Mn^{IV}, respectively. Thus, the electron transfer from S(IV) to Mn^{IV} and Mn^{III} led to the generation of Mn^{III} and Mn^{II}, respectively. Meanwhile, $SO_3^{\bullet-}$ was also generated in the solution. The Mn species within the catalyst, such as Mn^{II} and Mn^{III}, were oxidized by dissolved oxygen (equations (4) and (5)) or other oxygen species to Mn^{III} and Mn^{IV}, respectively. This indicates that the Mn(II) ↔ Mn(III) ↔ Mn(IV) redox cycle was established in the S(IV) system. $SO_5^{\bullet-}$ was generated by the oxidation of $SO_3^{\bullet-}$ via dissolved oxygen according to equation (6). Meanwhile, $SO_4^{\bullet-}$ was produced by the reaction of $SO_5^{\bullet-}$ with SO_3^{2-} (equation (7)) and by the internal electron transfer of $SO_5^{\bullet-}$ (equation (8)) [43]. The produced $SO_4^{\bullet-}$ then reacted with SO_3^{2-} to generate $SO_3^{\bullet-}$ (equation (9)), and $^{\bullet}OH$ was produced by the reaction of $SO_4^{\bullet-}$ with $^-OH/H_2O$ (equations (10) and

(11)). This indicates that the Mn_2O_3@Mn_5O_8/S(IV) system involved cyclic oxysulfur radical formation ($SO_3^{\bullet-}$, $SO_5^{\bullet-}$, and $SO_4^{\bullet-}$) as shown in Fig. 8. The multivalent Mn species in the Mn_2O_3@Mn_5O_8 yolk/shell structure along with monoclinic Mn_5O_8 and cubic Mn_2O_3 maintained the redox cycle and facilitated electron transfer; thus, the catalyst demonstrated effective catalytic performance. Overall, an appropriate combination of catalytic features was generated on Mn_2O_3@Mn_5O_8, which facilitated S(IV) activation to produce a large number of radicals for contaminant degradation.

$$\equiv Mn(II/III/IV)–OH + SO_3^{2-} \rightarrow \equiv Mn(II/III/IV)– SO_3^{-} + {}^{-}OH \quad (2)$$

$$\equiv Mn(II/III/IV)–SO_3^{-} + SO_3^{2-} \rightarrow \equiv Mn(II/III/IV)– SO_3^{-} + SO_3^{\bullet-} \quad (3)$$

$$\equiv Mn(II) + [O] + H^{+} \rightarrow \equiv Mn(III) + {}^{-}OH \quad (4)$$

$$\equiv Mn(III) + [O] + H^{+} \rightarrow \equiv Mn(IV) + {}^{-}OH \quad (5)$$

$$SO_3^{\bullet-} + O_2 \rightarrow SO_5^{\bullet-} \quad (6)$$

$$SO_5^{\bullet-} + SO_3^{2-} \rightarrow SO_4^{2-} + SO_4^{\bullet-} \quad (7)$$

$$SO_5^{\bullet-} + SO_5^{\bullet-} \rightarrow O_2 + 2SO_4^{\bullet-} \quad (8)$$

$$SO_4^{\bullet-} + SO_3^{2-} \rightarrow SO_4^{2-} + SO_3^{\bullet-} \quad (9)$$

$$SO_4^{\bullet-} + {}^{-}OH \rightarrow SO_4^{2-} + \bullet OH \quad (10)$$

$$SO_4^{\bullet-} + H_2O \rightarrow SO_4^{2-} + \bullet OH + H^{+} \quad (11)$$

3.7. Density functional theory (DFT) calculations

To compare and validate our experimental data, DFT studies were performed using 2D slab models of Mn_2O_3(001), Mn_5O_8(100), and Mn_2O_3@Mn_5O_8(100). Both pristine and 2% oxygen-

deficient surfaces of these species were considered, and the catalytic efficiency was predicted in the form of adsorption energy based on the interaction with –OH groups. The per-OH adsorption energy over the pristine and oxygen-deficient surfaces of Mn_2O_3, Mn_5O_8, and Mn_2O_3@Mn_5O_8 were calculated using equation (12) and the values are listed in Table S2.

$$\Delta E_{ad} = E_{surface@OH} - (E_{OH} + E_{surface}) \quad (12)$$

where ΔE_{ad} is the adsorption energy, $E_{surface}$ is the energy of the clean surface, E_{OH} is the total free energy of OH, and $E_{surface@OH}$ is the energy of the optimized OH–slab complex. The optimized structures of Mn_2O_3, Mn_5O_8, and Mn_2O_3@Mn_5O_8 and their 2% oxygen-deficient species are shown in Figs. 9, S13, and S14. The interaction between O of –OH and the surface Mn atoms is also shown. The –OH groups interact with Mn atoms and form strong O–Mn bonds on the 2% oxygen-deficient surfaces, while they only weakly bond with the pristine surfaces.

Comparative analyses of the data in Table S2 indicate that –OH adsorption should be more favorable on oxygen-deficient surfaces than their pristine counterparts. Indeed, the highest adsorption energy was observed for the O_v-Mn_2O_3@Mn_5O_8(100)–OH surface (approximately −5.51 eV). This statement strongly corroborates our experimental results and confirms the significant finding that the presence of surface –OH groups enhances the catalytic efficiency of the Mn_2O_3@Mn_5O_8 heterostructure. This strong interaction energy is caused by strong bonding between the O of the –OH group and the surface metal atoms, as can be visualized from the ELF map in Fig. 10. The ELF maps of Mn_2O_3(001), Mn_5O_8(100), O_v-Mn_2O_3(001), and O_v-Mn_5O_8(100), with and without –OH interaction, are shown in Figs. S15 and S16.

The –OH adsorption on the Mn_2O_3@Mn_5O_8(100) surface is further enhanced by significant inter-charge transfer, as shown in the EDD images in Fig. S17. The contours of the electron cloud

density of Mn_2O_3@Mn_5O_8(100) are prominently changed due to the change in the oxidation state of the Mn atoms, as clearly highlighted by the red shaded area in the EDD image of O_v-Mn_2O_3@Mn_5O_8(100) (Fig. S17). The 2D plot of EDD along the *c*-axes of Mn_2O_3@Mn_5O_8(100), O_v-Mn_2O_3@Mn_5O_8(100), and their OH-interacted systems are shown in Figs. 11a and 12b, respectively. It is found that upon interaction with the –OH group, the change in EDD of the O_v-Mn_2O_3@Mn_5O_8(100) species is higher than that of the Mn_2O_3@Mn_5O_8(100) species, as can be observed from Figs. 11a and 12b. In these figures, the yellow and green areas denote electron accumulation and electron donation, respectively. A significant amount of inter-charge exchange occurred within the O_v-Mn_2O_3@Mn_5O_8(100) system, which is responsible for the adsorption of more –OH groups and efficient catalytic ability.

The DFT calculations indicated that the adsorption energy of –OH on the O_v-Mn_2O_3@Mn_5O_8(100) surface was about twice that on the pristine Mn_2O_3 and Mn_5O_8 surfaces. Consequently, more –OH groups will adsorb to the O_v-Mn_2O_3@Mn_5O_8(100) surface. The stronger the adsorption energy, the higher the catalytic activity. Finally, the oxygen-deficient O_v-Mn_2O_3@Mn_5O_8(100) system has a lower work function (4.74 eV) than that of the pristine Mn_2O_3@Mn_5O_8(100) system (4.79 eV), as shown in Figs. 11c and 11d. The lower the work function of a catalyst, the higher the electron transformation and catalytic activity. Thus, it was concluded that the Mn_2O_3@Mn_5O_8 catalyst provides more –OH groups, which act as active sites for S(IV) activation, and a higher electron transfer. Consequently, Mn_2O_3@Mn_5O_8 is highly suited to efficient catalysis.

3.8. Effects of reaction conditions on the degradation of phenol

3.8.1. Effect of the initial pH of the reaction solution

The preliminary pH of the reaction solution plays a vital role in the degradation of organic pollutants in aqueous media. Metal-based catalysts, such as $NiFe_2O_4$ and $CoFe_2O_4$, reportedly exhibit sluggish catalytic performance in sulfite systems at a low or neutral pH [6,9]. Experiments were conducted at the preliminary pH values of 3.0, 4.0, 5.0, 6.0, 7.0, 9.0, and 10.0 to investigate the effect of pH on the removal of phenol by the Mn_2O_3@Mn_5O_8/S(IV) system (Fig. 12a). The primary pH of the reaction solution was adjusted to the target pH using NaOH and H_2SO_4 after the addition of S(IV). The Mn_2O_3@Mn_5O_8/S(IV) system exhibited almost 100% phenol degradation within 60 and 150 min at the pH values of 3.0 and 4.0, respectively, whereas 91.0%, 82.0%, and 77.0% of phenol was removed within 180 min at the pH values of 5.0, 6.0, and 7.0, respectively. When the initial pH of the reaction solution was increased to 9.0 and 10.0, the phenol degradation rate decreased rapidly to 18% and 15% within 180 min, respectively. This observation indicates that the removal of phenol by the Mn_2O_3@Mn_5O_8/S(IV) system under the low-acidic and neutral pH conditions was higher than that under the alkaline conditions. Further experiments were conducted to examine the performance of Mn_2O_3@Mn_5O_8 alone for phenol removal at various pH values under identical conditions. Nearly 99% of phenol was eliminated by Mn_2O_3@Mn_5O_8 alone within 90 min at pH = 3.0, whereas only 23% and 9% of phenol was eliminated within 180 min at pH = 4.0 and 5.0, respectively, and less than 6% of phenol was removed within 180 min at pH = 6.0–10.0 (Fig. 12b). The phenol degradation capability of Mn_2O_3@Mn_5O_8 alone can be attributed to the oxidation of phenol via the Mn species in Mn_2O_3@Mn_5O_8, which is consistent with a previous report [34]. Furthermore, we noted that the phenol oxidation process by Mn_2O_3@Mn_5O_8 alone was very slow at pH 5 compared to that at pH 3, suggesting that in the Mn_2O_3@Mn_5O_8/S(IV) system, almost all the phenol degradation at pH 5.0–7.0 occurred through the radical process (Figs. 4a and 12a).

The zero-point charge (ZPC) of Mn_2O_3@Mn_5O_2 was calculated to be approximately 3.4 (Fig. 12c). The Mn_2O_3@Mn_5O_8 surface was positively charged when pH < pH_{zpc}, whereas it was negatively charged when pH > pH_{zpc} [40,53]. The pKa value of S(IV) is 7.2 [43]. This finding indicates that when the pH was below 3.4, Mn_2O_3@Mn_5O_8 was positively charged, which increased the reaction rate with negatively charged S(IV) (SO_3^{-2}) and accelerated the activation of S(IV). This increased the degradation of phenol. This phenomenon is in agreement with the previous studies on the activation of persulfate by Mn-based catalysts [40,53] and implies that an increase in the electrostatic repulsion force may decrease the interactions between Mn_2O_3@Mn_5O_2 and S(IV), thereby hindering the phenol degradation. Furthermore, at high pH values of 9.0 and 10.0 that are close to the pKa value of phenol (10.0), almost all of the pollutants were deprotonated and negatively charged; consequently, the interaction between phenol and the catalyst was reduced, accounting for the suppressed phenol degradation.

3.8.2. Influence of Mn_2O_3@Mn_5O_8 dosage and S(IV) concentration

Figs. 13a and b show the effects of Mn_2O_3@Mn_5O_8 dosage and S(IV) concentration on the degradation of phenol. When 0.2 or 0.3 g L^{-1} Mn_2O_3@Mn_5O_8 was used, 91% and 98% of phenol, respectively, were removed in 180 min; in contrast, when 0.1 g L^{-1} Mn_2O_3@Mn_5O_8 was employed, 68% of phenol was eliminated within 180 min (Fig. 13a). This result demonstrates that the number of active sites increases with the Mn_2O_3@Mn_5O_8 dosage because of the substantial activation of S(IV) [11,24]. S(IV) in various concentrations was used in the presence of Mn_2O_3@Mn_5O_8 to analyze the influence of S(IV) concentration on the degradation of phenol (Fig. 13b). S(IV) in concentrations ranging from 0.2 to 0.7 mM led to significantly high eliminations of phenol. However, a further increase in S(IV) concentration to 1 mM caused the removal of phenol to

512 decrease, as compared to that observed with 0.7 mM. This observation indicates that excessive
513 S(IV) quenches the ROS and reduces the phenol removal rate [6].

514 ***3.8.3. Effect of anions and HA***

515 The contents of various anions in the Mn_2O_3@Mn_5O_8/S(IV) system, including CO_3^{2-}, Cl^-, NO_3^-,
516 and SO_4^- (5 mM), were determined to investigate their influence and interaction, as shown in Fig.
517 13c. Inorganic anions commonly exist in aqueous media and can act as scavengers for radical-
518 based oxidation. In addition, they often reduce the degradation performance of AOPs. For instance,
519 $SO_4^{\bullet-}$and •OH radicals can be scavenged by CO_3^{2-} with the rate constants, *k*, of 6.1×10^6 and $3 \times$
520 10^8 M^{-1} s^{-1}, respectively, generating less reactive $\bullet CO_3^-$ radicals (equations (13) and (14)) [54,55].
521 In the present study, when CO_3^{2-} was introduced into the Mn_2O_3@Mn_5O_8/S(IV) system at pH =
522 5, the degradation rate of phenol decreased from 91% to 34%. This implies that the $SO_4^{\bullet-}$ and/or
523 •OH radicals were scavenged by CO_3^{2-}. Therefore, •OH was dominant in the S(IV) system, and
524 the addition of CO_3^{2-} decreased the degradation rate of phenol. In the presence of Cl^-, the phenol
525 elimination rate decreased from 91% to 64%, demonstrating some $SO_4^{\bullet-}$ and/or •OH radical
526 scavenging was performed by Cl^-. It has been reported that $SO_4^{\bullet-}$ and •OH react with Cl^- with the
527 reaction rate constants, *k*, of 3.2×10^8 and 4.2×10^9 M^{-1} s^{-1}, respectively, generating •Cl radicals
528 ($E_{0(\bullet Cl_2/2Cl^-)}$ = 2.40 V), as shown in equations (15) and (16) [54,56]. As a result, the presence of
529 Cl^- may decrease the phenol degradation rate. Similarly, when NO_3^- was added to the reaction
530 solution, the phenol degradation rate decreased from 91% to 72%, suggesting that a reaction
531 occurred between the $SO_4^{\bullet-}$ and/or •OH radicals and NO_3^- to produce less reactive $NO_3^{\bullet}$ radicals
532 (equations (17) and (18)) [54]. When SO_4^{2-} was introduced into the same system, the degradation
533 rate of phenol decreased slightly (91% to 83%), indicating that this anion had lesser effect on the
534 degradation of phenol. Thus, several anions have negative effects on the phenol degradation

efficiency. This suggests that the Mn_2O_3@Mn_5O_8/S(IV) system produces various radicals, which can react with anions and generate less reactive species, and ultimately deteriorate the phenol degradation performance. Further degradation experiments were conducted at pH = 5 to study the performance of the Mn_2O_3@Mn_5O_8/S(IV) system in the presence of HA to investigate the influence of natural organic matter. As shown in Fig. 13d, as the amount of HA increased from 0 to 10 mg L^{-1}, the elimination rate of phenol decreased from 91% to 70% within 180 min. This decrease in the removal rate of phenol with a large addition of HA may be related to the scavenging ability of HA, which created competition for the radicals with the target compound [55].

$$CO_3^{2-} + SO_4^{\bullet-} \rightarrow CO_3^{\bullet-} + SO_4^{2-} \quad (13)$$

$$CO_3^{2-} + \bullet OH \rightarrow CO_3^{\bullet-} + OH^- \quad (14)$$

$$Cl^- + SO_4^{\bullet-} \rightarrow SO_4^{2-} + \bullet Cl \quad (15)$$

$$Cl^- + \bullet OH \rightarrow OH^- + \bullet Cl \quad (16)$$

$$NO_3^- + SO_4^{\bullet-} \rightarrow SO_4^{2-} + NO_3^{\bullet} \quad (17)$$

$$NO_3^- + \bullet OH \rightarrow OH^- + NO_3^{\bullet} \quad (18)$$

3.9. Mineralization

The mineralization of phenol in the Mn_2O_3@Mn_5O_8/S(IV) system was studied to investigate the TOC levels in the sample. Around 32% TOC removal was observed when 91% of phenol was degraded within 180 mins (Fig. S18). Most metal-based or composite catalysts cause slight mineralization of the organic contaminants in the S(IV) system [16,57]. However, the Mn_2O_3@Mn_5O_8/S(IV) system not only showed efficient degradation of phenol in water but also the removal of generated intermediates during the reaction, which could be very favorable for wastewater treatment. The efficient mineralization of organic pollutants in the

557 Mn_2O_3@Mn_5O_8/S(IV) system may be attributed to the high content of •OH radicals, as shown in
558 Fig. 5a. The oxidation of almost any compound occurs through •OH radicals, which are excellent
559 for their non-selectivity toward the substrate. Consequently, •OH radicals contribute to efficient
560 mineralization [57]. In contrast, $SO_4^{\bullet-}$ radicals are excellent for their strong selectivity toward a
561 target compound [58,59]. They can generate recalcitrant products during the degradation process,
562 which cannot be further degraded by $SO_4^{\bullet-}$/$SO_5^{\bullet-}$ [57]. Thus, the combined effect of $SO_4^{\bullet-}$ and
563 •OH radicals provides efficient mineralization of phenol, which is significant for the removal of
564 contaminants as well as generated intermediates in aqueous media.

565 **4. Conclusions**

566 Herein, the catalytic performance of Mn_2O_3@Mn_5O_8, α-MnO_2, Mn_2O_3, Mn_3O_4, Mn_5O_8, and other
567 transition-metal oxides (CuO, Co_3O_4, and Fe_2O_3) toward phenol degradation were investigated in
568 a S(IV) system. The following conclusions were drawn from the results of this study:

569 • Mn_2O_3@Mn_5O_8 can be more facilely synthesized than other Mn oxides and shows better
570 catalytic performance than other S(IV) activators, which is attributed to its unique
571 architecture, multivalent states, surface hydroxyl groups (–OH), and large surface area. The
572 efficient redox conversion of Mn species (Mn(II) ↔Mn(III) ↔Mn(IV)) is promoted by
573 Mn_2O_3@Mn_5O_8 during the catalytic reaction.
574 • DFT simulations reveal that O_v-Mn_2O_3@Mn_5O_8(100) has a higher catalytic activity than
575 that of Mn_2O_3 and Mn_5O_8as as indicated by a strong –OH adsorption energy and significant
576 inter-charge transformation.
577 • Various experiments suggested that S(IV) is activated by Mn_2O_3@Mn_5O_8 that generates
578 $SO_3^{\bullet-}$, $SO_5^{\bullet-}$, $SO_4^{\bullet-}$, and $^{\bullet}$OH radicals, with $SO_3^{\bullet-}$ acting as the precursor for the production
579 of other radicals.

- Radical-scavenging experiments confirmed that phenol is mainly removed by $^{\bullet}OH$ and is partially removed by $SO_4^{\bullet-}$ and $SO_5^{\bullet-}$ radicals.
- At an initial solution pH of 3.0–7.0, the best degradation of phenol is achieved, whereas the phenol degradation rate decreases at higher pH. The phenol elimination performance of Mn_2O_3@Mn_5O_8 varies depending on the presence of other inorganic anions, whereas TOC degradation is efficient in the S(IV) system.
- Due to the low toxicity of Mn_2O_3@Mn_5O_8 and its high S(IV) activation ability, our method can be considered a green approach for environmental remediation as compared to the conventional methods.

Acknowledgments

The authors are grateful for the funding provided by the National Natural Science Foundation of China (51978542) and Hubei Key Laboratory of Biomass Fibers & Eco-Dyeing & Finishing (Wuhan Textile University).

References

[1] J. Wang, S. Wang, Activation of persulfate (PS) and peroxymonosulfate (PMS) and application for the degradation of emerging contaminants, Chemical Engineering Journal. 334 (2018) 1502–1517. https://doi.org/10.1016/j.cej.2017.11.059.

[2] Q. Liu, X. Duan, H. Sun, Y. Wang, M.O. Tade, S. Wang, Size-tailored porous spheres of manganese oxides for catalytic oxidation via peroxymonosulfate activation, Journal of Physical Chemistry C. 120 (2016) 16871–16878. https://doi.org/10.1021/acs.jpcc.6b05934.

[3] N. Tian, X. Tian, Y. Nie, C. Yang, Z. Zhou, Y. Li, Biogenic manganese oxide: An efficient peroxymonosulfate activation catalyst for tetracycline and phenol degradation in water, Chemical Engineering Journal. 352 (2018) 469–476. https://doi.org/10.1016/j.cej.2018.07.061.

[4] C. Yin, A. Khan, Q. Gao, Q. Li, X. Zhou, X. Liu, A. Xu, X. Li, Synergistic activation of peroxymonosulfate for efficient aqueous p-nitrophenol degradation with Cu(II) and Ag(I) in Ag2Cu2O3, Separation and Purification Technology. 291 (2022). https://doi.org/10.1016/j.seppur.2022.120934.

[5] Y. Zhao, H. Dai, J. Ji, X. Yuan, X. Li, L. Jiang, H. Wang, Resource utilization of luffa sponge to produce biochar for effective degradation of organic contaminants through persulfate activation, Separation and Purification Technology. 288 (2022). https://doi.org/10.1016/j.seppur.2022.120650.

[6] Y. Chen, M. Li, Y. Tong, Z. Liu, L. Fang, Y. Wu, Z. Fang, F. Wu, L.Z. Huang, Radical generation via sulfite activation on NiFe2O4 surface for estriol removal: Performance and mechanistic studies, Chemical Engineering Journal. 368 (2019). https://doi.org/10.1016/j.cej.2019.02.196.

[7] H. Lin, J. Wu, H. Zhang, Degradation of clofibric acid in aqueous solution by an EC/Fe3+/PMS process, Chemical Engineering Journal. 244 (2014). https://doi.org/10.1016/j.cej.2014.01.099.

[8] K.S. Sra, N.R. Thomson, J.F. Barker, Persistence of persulfate in uncontaminated aquifer materials, Environmental Science and Technology. 44 (2010). https://doi.org/10.1021/es903480k.

[9] Z. Liu, S. Yang, Y. Yuan, J. Xu, Y. Zhu, J. Li, F. Wu, A novel heterogeneous system for sulfate radical generation through sulfite activation on a CoFe2O4 nanocatalyst surface, Journal of Hazardous Materials. 324 (2017). https://doi.org/10.1016/j.jhazmat.2016.11.029.

[10] Z. Shi, C. Jin, J. Zhang, L. Zhu, Insight into mechanism of arsanilic acid degradation in permanganate-sulfite system: Role of reactive species, Chemical Engineering Journal. 359 (2019). https://doi.org/10.1016/j.cej.2018.11.030.

[11] W. Ding, W. Xiao, W. Huang, Q. Sun, H. Zheng, Sulfite activation on a silica-supported well-dispersed cobalt catalyst via an electron transfer complex path, Journal of Cleaner Production. 257 (2020). https://doi.org/10.1016/j.jclepro.2020.120457.

[12] D. Wu, P. Ye, M. Wang, Y. Wei, X. Li, A. Xu, Cobalt nanoparticles encapsulated in nitrogen-rich carbon nanotubes as efficient catalysts for organic pollutants degradation via sulfite activation, Journal of Hazardous Materials. 352 (2018). https://doi.org/10.1016/j.jhazmat.2018.03.040.

[13] J. Zhang, L. Zhu, Z. Shi, Y. Gao, Rapid removal of organic pollutants by activation sulfite with ferrate, Chemosphere. 186 (2017). https://doi.org/10.1016/j.chemosphere.2017.07.102.

[14] B. Jiang, X. Wang, Y. Liu, Z. Wang, J. Zheng, M. Wu, The roles of polycarboxylates in Cr(VI)/sulfite reaction system: Involvement of reactive oxygen species and intramolecular electron transfer, Journal of Hazardous Materials. 304 (2016). https://doi.org/10.1016/j.jhazmat.2015.11.011.

[15] Y. Yuan, T. Luo, J. Xu, J. Li, F. Wu, M. Brigante, G. Mailhot, Enhanced oxidation of aniline using Fe(III)-S(IV) system: Role of different oxysulfur radicals, Chemical Engineering Journal. 362 (2019). https://doi.org/10.1016/j.cej.2019.01.010.

[16] L. Chen, X. Peng, J. Liu, J. Li, F. Wu, Decolorization of orange ii in aqueous solution by an Fe(II)/sulfite system: Replacement of persulfate, Industrial and Engineering Chemistry Research. 51 (2012). https://doi.org/10.1021/ie3020389.

[17] M. ben Ali, A. Barras, A. Addad, B. Sieber, H. Elhouichet, M. Férid, S. Szunerits, R. Boukherroub, Co2SnO4 nanoparticles as a high performance catalyst for oxidative degradation of rhodamine B

dye and pentachlorophenol by activation of peroxymonosulfate, Physical Chemistry Chemical Physics. 19 (2017) 6569–6578. https://doi.org/10.1039/c6cp08576h.

[18] A. Khan, Z. Liao, Y. Liu, A. Jawad, J. Ifthikar, Z. Chen, Synergistic degradation of phenols using peroxymonosulfate activated by CuO-Co3O4@MnO2 nanocatalyst, Journal of Hazardous Materials. 329 (2017) 262–271. https://doi.org/10.1016/j.jhazmat.2017.01.029.

[19] J. Du, J. Bao, Y. Liu, S.H. Kim, D.D. Dionysiou, Facile preparation of porous Mn/Fe3O4 cubes as peroxymonosulfate activating catalyst for effective bisphenol A degradation, Chemical Engineering Journal. 376 (2019). https://doi.org/10.1016/j.cej.2018.05.177.

[20] R. Yuan, Z. Jiang, Z. Wang, S. Gao, Z. Liu, M. Li, G. Boczkaj, Hierarchical MnO2 nanoflowers blooming on 3D nickel foam: A novel micro-macro catalyst for peroxymonosulfate activation, Journal of Colloid and Interface Science. 571 (2020) 142–154. https://doi.org/10.1016/j.jcis.2020.03.041.

[21] J.C.E. Yang, Y. Lin, H.H. Peng, B. Yuan, D.D. Dionysiou, X.D. Huang, D.D. Zhang, M.L. Fu, Novel magnetic rod-like Mn-Fe oxycarbide toward peroxymonosulfate activation for efficient oxidation of butyl paraben: Radical oxidation versus singlet oxygenation, Applied Catalysis B: Environmental. 268 (2020). https://doi.org/10.1016/j.apcatb.2019.118549.

[22] A. Khan, H. Wang, Y. Liu, A. Jawad, J. Ifthikar, Z. Liao, T. Wang, Z. Chen, Highly efficient α-Mn2O3α-MnO2-500 nanocomposite for peroxymonosulfate activation: Comprehensive investigation of manganese oxides, Journal of Materials Chemistry A. 6 (2018) 1590–1600. https://doi.org/10.1039/c7ta07942g.

[23] E. Saputra, H. Zhang, Q. Liu, H. Sun, S. Wang, Egg-shaped core/shell α-Mn2O3@α-MnO2 as heterogeneous catalysts for decomposition of phenolics in aqueous solutions, Chemosphere. 159 (2016) 351–358. https://doi.org/10.1016/j.chemosphere.2016.06.021.

[24] E. Saputra, S. Muhammad, H. Sun, H.M. Ang, M.O. Tadé, S. Wang, Manganese oxides at different oxidation states for heterogeneous activation of peroxymonosulfate for phenol degradation in aqueous solutions, Applied Catalysis B: Environmental. 142–143 (2013) 729–735. https://doi.org/10.1016/j.apcatb.2013.06.004.

[25] Y. Zhao, H. An, J. Feng, Y. Ren, J. Ma, Impact of Crystal Types of AgFeO2 Nanoparticles on the Peroxymonosulfate Activation in the Water, Environmental Science and Technology. 53 (2019) 4500–4510. https://doi.org/10.1021/acs.est.9b00658.

[26] E. Saputra, S. Muhammad, H. Sun, H.M. Ang, M.O. Tadé, S. Wang, Different crystallographic one-dimensional MnO2 nanomaterials and their superior performance in catalytic phenol degradation, Environmental Science and Technology. 47 (2013) 5882–5887. https://doi.org/10.1021/es400878c.

[27] J. Yu, T. Zeng, H. Wang, H. Zhang, Y. Sun, L. Chen, S. Song, L. Li, H. Shi, Oxygen-defective MnO2−x rattle-type microspheres mediated singlet oxygen oxidation of organics by peroxymonosulfate activation, Chemical Engineering Journal. 394 (2020). https://doi.org/10.1016/j.cej.2020.124458.

[28] Z.M. Cui, Z. Chen, C.Y. Cao, L. Jiang, W.G. Song, A yolk–shell structured Fe2O3@mesoporous SiO2 nanoreactor for enhanced activity as a Fenton catalyst in total oxidation of dyes, Chemical Communications. 49 (2013) 2332–2334. https://doi.org/10.1039/c3cc38649j.

[29] A. Khan, K. Zhang, A. Taraqqi-A-Kamal, X. Wang, Y. Chen, Y. Zhang, Degradation of antibiotics in aqueous media using manganese nanocatalyst-activated peroxymonosulfate, Journal of Colloid and Interface Science. 599 (2021). https://doi.org/10.1016/j.jcis.2021.04.095.

[30] W. da Oh, Z. Dong, T.T. Lim, Generation of sulfate radical through heterogeneous catalysis for organic contaminants removal: Current development, challenges and prospects, Applied Catalysis B: Environmental. 194 (2016) 169–201. https://doi.org/10.1016/j.apcatb.2016.04.003.

[31] A. Khan, S. Zou, T. Wang, J. Ifthikar, A. Jawad, Z. Liao, A. Shahzad, A. Ngambia, Z. Chen, Facile synthesis of yolk shell Mn2O3@Mn5O8 as an effective catalyst for peroxymonosulfate activation, Physical Chemistry Chemical Physics. 20 (2018) 13909–13919. https://doi.org/10.1039/c8cp02080a.

[32] D. Jeong, K. Jin, S.E. Jerng, H. Seo, D. Kim, S.H. Nahm, S.H. Kim, K.T. Nam, Mn5O8 Nanoparticles as Efficient Water Oxidation Catalysts at Neutral pH, ACS Catalysis. 5 (2015). https://doi.org/10.1021/acscatal.5b01269.

[33] Y. Wang, H. Sun, H.M. Ang, M.O. Tadé, S. Wang, 3D-hierarchically structured MnO2 for catalytic oxidation of phenol solutions by activation of peroxymonosulfate: Structure dependence and mechanism, Applied Catalysis B: Environmental. 164 (2015) 159–167. https://doi.org/10.1016/j.apcatb.2014.09.004.

[34] B. Sun, Z. Xiao, H. Dong, S. Ma, G. Wei, T. Cao, X. Guan, Bisulfite triggers fast oxidation of organic pollutants by colloidal MnO2, Journal of Hazardous Materials. 363 (2019). https://doi.org/10.1016/j.jhazmat.2018.10.002.

[35] T. Zhang, Y. Chen, Y. Wang, J. le Roux, Y. Yang, J.P. Croué, Efficient peroxydisulfate activation process not relying on sulfate radical generation for water pollutant degradation, Environmental Science and Technology. 48 (2014) 5868–5875. https://doi.org/10.1021/es501218f.

[36] S. Smidstrup, T. Markussen, P. Vancraeyveld, J. Wellendorff, J. Schneider, T. Gunst, B. Verstichel, D. Stradi, P.A. Khomyakov, U.G. Vej-Hansen, M.E. Lee, S.T. Chill, F. Rasmussen, G. Penazzi, F. Corsetti, A. Ojanperä, K. Jensen, M.L.N. Palsgaard, U. Martinez, A. Blom, M. Brandbyge, K. Stokbro, QuantumATK: An integrated platform of electronic and atomic-scale modelling tools, Journal of Physics Condensed Matter. 32 (2020). https://doi.org/10.1088/1361-648X/ab4007.

[37] A. Khan, K. Zhang, P. Sun, H. Pan, Y. Cheng, Y. Zhang, High performance of the A-Mn2O3 nanocatalyst for persulfate activation: Degradation process of organic contaminants via singlet oxygen, Journal of Colloid and Interface Science. 584 (2021) 885–899. https://doi.org/10.1016/j.jcis.2020.10.021.

[38] H. Liang, H. Sun, A. Patel, P. Shukla, Z.H. Zhu, S. Wang, Excellent performance of mesoporous Co 3O 4/MnO 2 nanoparticles in heterogeneous activation of peroxymonosulfate for phenol degradation in aqueous solutions, Applied Catalysis B: Environmental. 127 (2012) 330–335. https://doi.org/10.1016/j.apcatb.2012.09.001.

[39] L. Cheng, Y. Men, J. Wang, H. Wang, W. An, Y. Wang, Z. Duan, J. Liu, Crystal facet-dependent reactivity of α-Mn2O3 microcrystalline catalyst for soot combustion, Applied Catalysis B: Environmental. 204 (2017) 374–384. https://doi.org/10.1016/j.apcatb.2016.11.041.

[40] Z. Dong, Q. Zhang, B.Y. Chen, J. Hong, Oxidation of bisphenol A by persulfate via Fe3O4-A-MnO2 nanoflower-like catalyst: Mechanism and efficiency, Chemical Engineering Journal. 357 (2019) 337–347. https://doi.org/10.1016/j.cej.2018.09.179.

[41] Y. Xu, J. Ai, H. Zhang, The mechanism of degradation of bisphenol A using the magnetically separable CuFe2O4/peroxymonosulfate heterogeneous oxidation process, Journal of Hazardous Materials. 309 (2016) 87–96. https://doi.org/10.1016/j.jhazmat.2016.01.023.

[42] S. Zhu, X. Li, J. Kang, X. Duan, S. Wang, Persulfate Activation on Crystallographic Manganese Oxides: Mechanism of Singlet Oxygen Evolution for Nonradical Selective Degradation of Aqueous Contaminants, Environmental Science and Technology. 53 (2019) 307–315. https://doi.org/10.1021/acs.est.8b04669.

[43] L.Z. Huang, X. Wei, E. Gao, C. Zhang, X.M. Hu, Y. Chen, Z. Liu, N. Finck, J. Lützenkirchen, D.D. Dionysiou, Single Fe atoms confined in two-dimensional MoS2 for sulfite activation: A biomimetic approach towards efficient radical generation, Applied Catalysis B: Environmental. 268 (2020). https://doi.org/10.1016/j.apcatb.2019.118459.

[44] J. Du, W. Guo, H. Wang, R. Yin, H. Zheng, X. Feng, D. Che, N. Ren, Hydroxyl radical dominated degradation of aquatic sulfamethoxazole by Fe0/bisulfite/O2: Kinetics, mechanisms, and pathways, Water Research. 138 (2018). https://doi.org/10.1016/j.watres.2017.12.046.

[45] L. Wojnárovits, E. Takács, Rate constants of sulfate radical anion reactions with organic molecules: A review, Chemosphere. 220 (2019) 1014–1032. https://doi.org/10.1016/j.chemosphere.2018.12.156.

[46] Y. Zhang, W. Yang, K. Zhang, A. Kumaravel, Y. Zhang, Sulfite Activation by Glucose-Derived Carbon Catalysts for As(III) Oxidation: The Role of Ketonic Functional Groups and Conductivity, Environmental Science & Technology. 55 (2021). https://doi.org/10.1021/acs.est.1c02499.

[47] T. Gao, P. Norby, F. Krumeich, H. Okamoto, R. Nesper, H. Fjellvag, Synthesis and properties of layered-structured Mn5O8 nanorods, Journal of Physical Chemistry C. 114 (2010). https://doi.org/10.1021/jp9097606.

[48] Z. Xie, Z. Lyu, J. Wang, A. Li, P. François-Xavier Corvini, Ultrafine-Mn2O3@N-doped porous carbon hybrids derived from Mn-MOFs: Dual-reaction centre catalyst with singlet oxygen-dominant oxidation process, Chemical Engineering Journal. 429 (2022). https://doi.org/10.1016/j.cej.2021.132299.

[49] D. Hosseini, Q. Imtiaz, P.M. Abdala, S. Yoon, A.M. Kierzkowska, A. Weidenkaff, C.R. Müller, CuO promoted Mn2O3-based materials for solid fuel combustion with inherent CO2 capture, Journal of Materials Chemistry A. 3 (2015) 10545–10550. https://doi.org/10.1039/c5ta01088h.

[50] Y. Ren, L. Lin, J. Ma, J. Yang, J. Feng, Z. Fan, Sulfate radicals induced from peroxymonosulfate by magnetic ferrospinel MFe2O4 (M=Co, Cu, Mn, and Zn) as heterogeneous catalysts in the water,

Applied Catalysis B: Environmental. 165 (2015) 572–578. https://doi.org/10.1016/j.apcatb.2014.10.051.

[51] P. Duan, T. Ma, Y. Yue, Y. Li, X. Zhang, Y. Shang, B. Gao, Q. Zhang, Q. Yue, X. Xu, Fe/Mn nanoparticles encapsulated in nitrogen-doped carbon nanotubes as a peroxymonosulfate activator for acetamiprid degradation, Environmental Science: Nano. 6 (2019) 1799–1811. https://doi.org/10.1039/c9en00220k.

[52] X. Tan, Y. Wan, Y. Huang, C. He, Z. Zhang, Z. He, L. Hu, J. Zeng, D. Shu, Three-dimensional MnO2 porous hollow microspheres for enhanced activity as ozonation catalysts in degradation of bisphenol A, Journal of Hazardous Materials. 321 (2017) 162–172. https://doi.org/10.1016/j.jhazmat.2016.09.013.

[53] K.Z. Huang, H. Zhang, Direct Electron-Transfer-Based Peroxymonosulfate Activation by Iron-Doped Manganese Oxide (δ-MnO2) and the Development of Galvanic Oxidation Processes (GOPs), Environmental Science and Technology. 53 (2019) 12610–12620. https://doi.org/10.1021/acs.est.9b03648.

[54] S. Yan, X. Zhang, Y. Shi, H. Zhang, Natural Fe-bearing manganese ore facilitating bioelectro-activation of peroxymonosulfate for bisphenol A oxidation, Chemical Engineering Journal. 354 (2018) 1120–1131. https://doi.org/10.1016/j.cej.2018.08.066.

[55] J. Ali, L. Wenli, A. Shahzad, J. Ifthikar, G.G. Aregay, I.I. Shahib, Z. Elkhlifi, Z. Chen, Z. Chen, Regulating the redox centers of Fe through the enrichment of Mo moiety for persulfate activation: A new strategy to achieve maximum persulfate utilization efficiency, Water Research. 181 (2020). https://doi.org/10.1016/j.watres.2020.115862.

[56] Y. Feng, P.H. Lee, D. Wu, K. Shih, Surface-bound sulfate radical-dominated degradation of 1,4-dioxane by alumina-supported palladium (Pd/Al2O3) catalyzed peroxymonosulfate, Water Research. 120 (2017) 12–21. https://doi.org/10.1016/j.watres.2017.04.070.

[57] D. Zhou, L. Chen, J. Li, F. Wu, Transition metal catalyzed sulfite auto-oxidation systems for oxidative decontamination in waters: A state-of-the-art minireview, Chemical Engineering Journal. 346 (2018). https://doi.org/10.1016/j.cej.2018.04.016.

[58] J. Ai, Z. Wang, D.D. Dionysiou, M. Liu, Y. Deng, M. Tang, G. Liao, A. Hu, W. Zhang, Understanding synergistic mechanisms of ferrous iron activated sulfite oxidation and organic polymer flocculation for enhancing wastewater sludge dewaterability, Water Research. 189 (2021). https://doi.org/10.1016/j.watres.2020.116652.

[59] S. Luo, Z. Wei, D.D. Dionysiou, R. Spinney, W.P. Hu, L. Chai, Z. Yang, T. Ye, R. Xiao, Mechanistic insight into reactivity of sulfate radical with aromatic contaminants through single-electron transfer pathway, Chemical Engineering Journal. 327 (2017) 1056–1065. https://doi.org/10.1016/j.cej.2017.06.179.

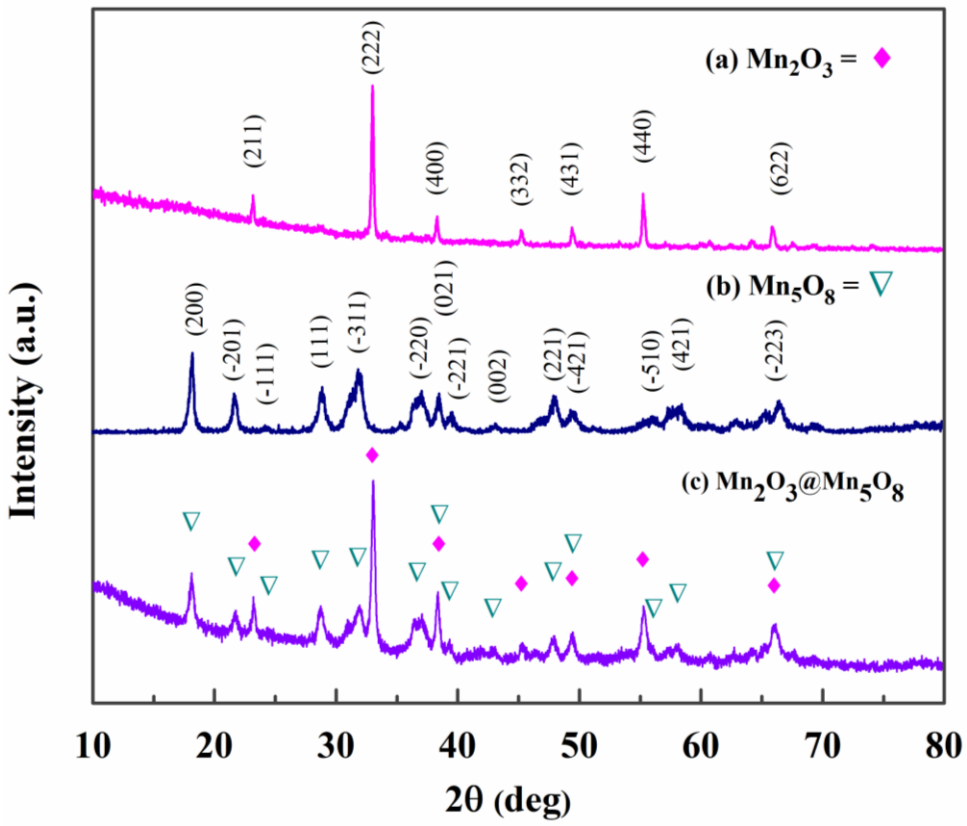

795

796 **Fig. 1.** XRD pattern of (a) Mn_2O_3, (b) Mn_5O_8, and (c) Mn_2O_3@Mn_5O_8.

797

798

799

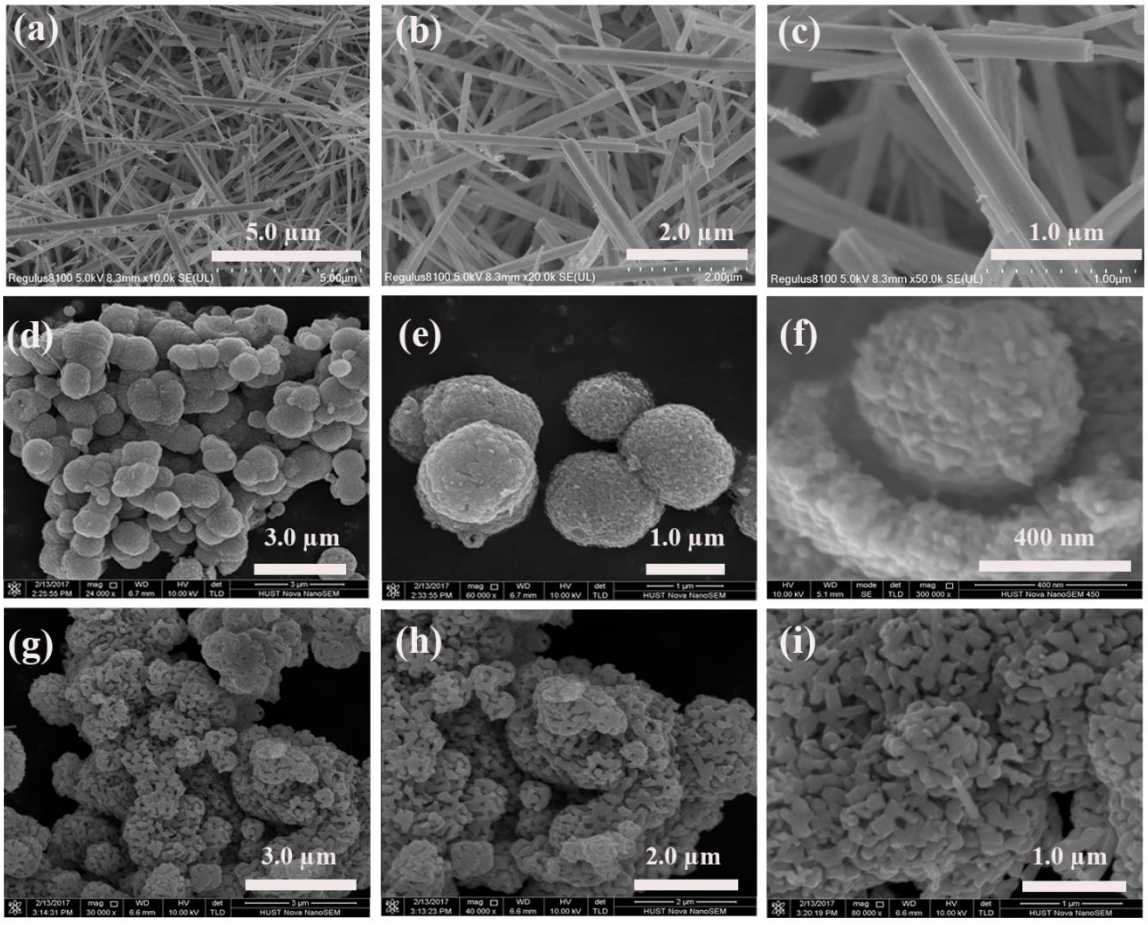

Fig. 2(a–i). Scanning electron microscopy (SEM) images of the as-prepared nanostructured materials: (a–c) Mn_5O_8, (d–f) Mn_2O_3@Mn_5O_8, and (g–i) Mn_2O_3.

805 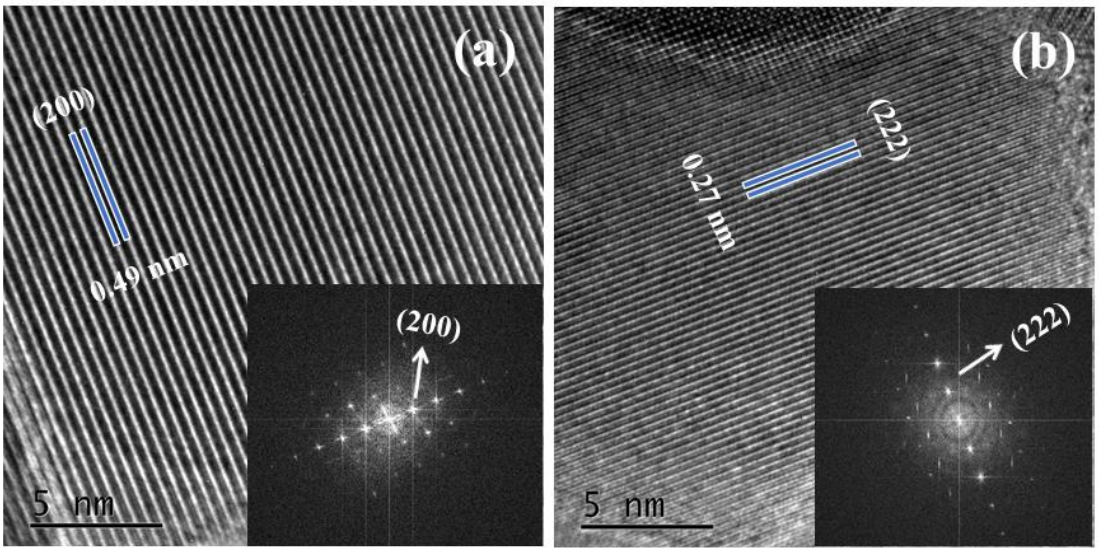

806 **Fig. 3. (a and b)** Structural characterizations of the Mn_2O_3@Mn_5O_8 material. **(a)** HRTEM image
807 of Mn_5O_8 and FFT inset in HRTEM images, **(b)** HRTEM image of Mn_2O_3 and FFT inset in
808 HRTEM images.

809

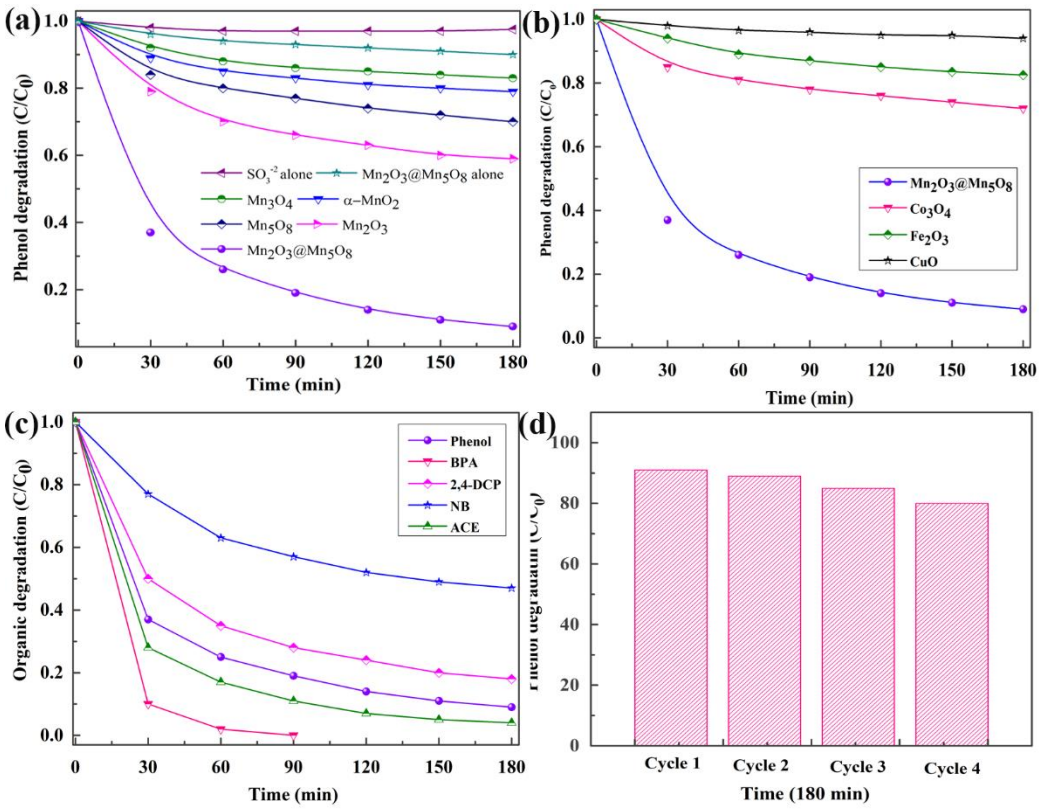

Fig. 4(a-d). (a and b) phenol degradation on various metal oxides, **(c)** Different organic degradation, **(d)** Stability of the $Mn_2O_3@Mn_5O_8$. Reaction conditions: Catalyst 0.2 g/L, sulfite 0.7 mM, contaminants 50 μM, and temperature: 30 ˚C.

821 **Table 1** Pseudo first order rate constant and BET values for various catalysts.

Entry	Catalyst	Rate constant (min^{-1})	Phenol removal (%)	BET (m^2/g)
1	Mn_2O_3@Mn_5O_8	0.0167	91	45.0
2	α-MnO_2	0.0017	21	22.4
3	Mn_2O_3	0.0040	41	32.0
4	Mn_3O_4	0.0014	17	21.0
5	Mn_5O_8	0.0025	30	11.0

822

823

824

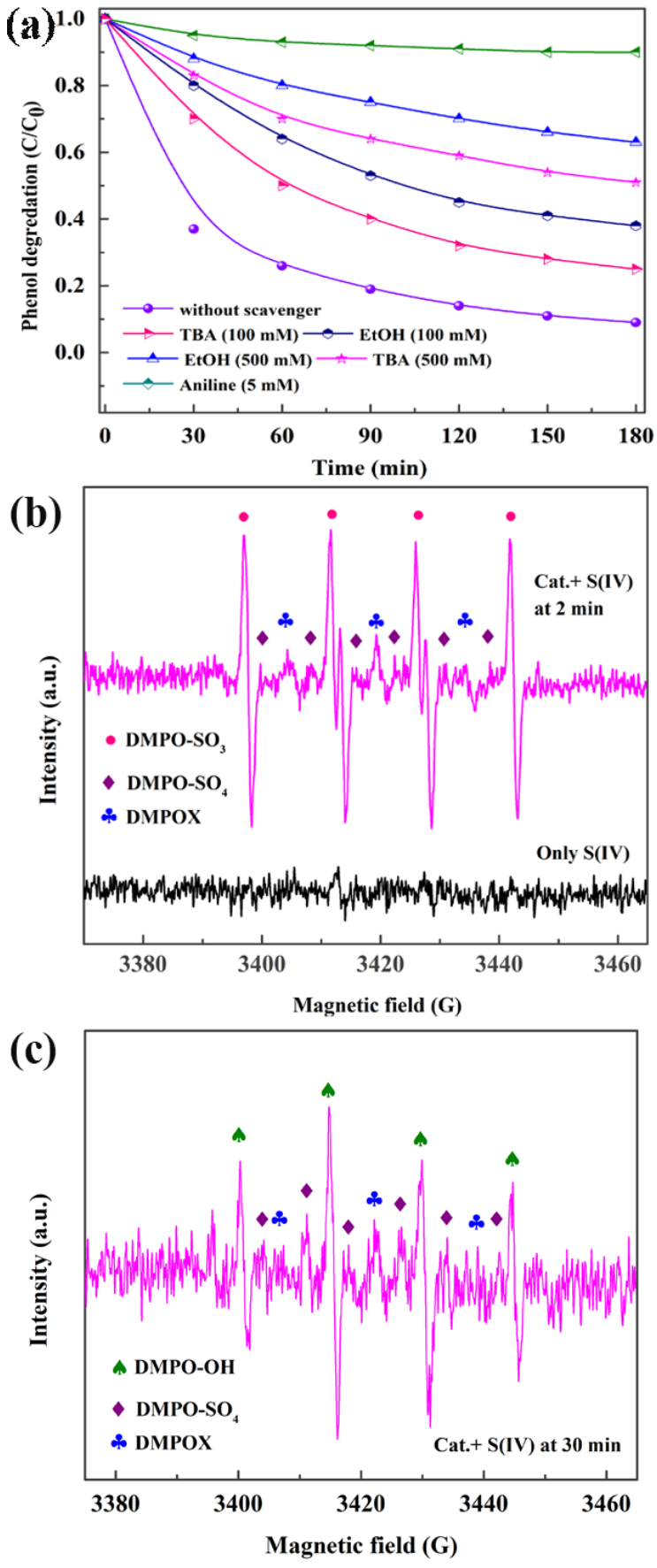

Fig. 5(a-c). (a) Inhibition of aniline, EtOH and TBA on the phenol degradation by Mn_2O_3@Mn_5O_8/S(IV). **(b and c)** DMPO spin-trapping EPR spectra using sulfite activated by Mn_2O_3@Mn_5O_8, ●: $SO_3^{\bullet-}$, ♦: $SO_4^{\bullet-}$, ♠: •OH, ♣: DMPOX, Reaction conditions: catalyst 0.2 g L^{-1}, sulfite 0.7 mM, phenol 50 μM, temperature: 30 ˚C and DMPO 50 mM.

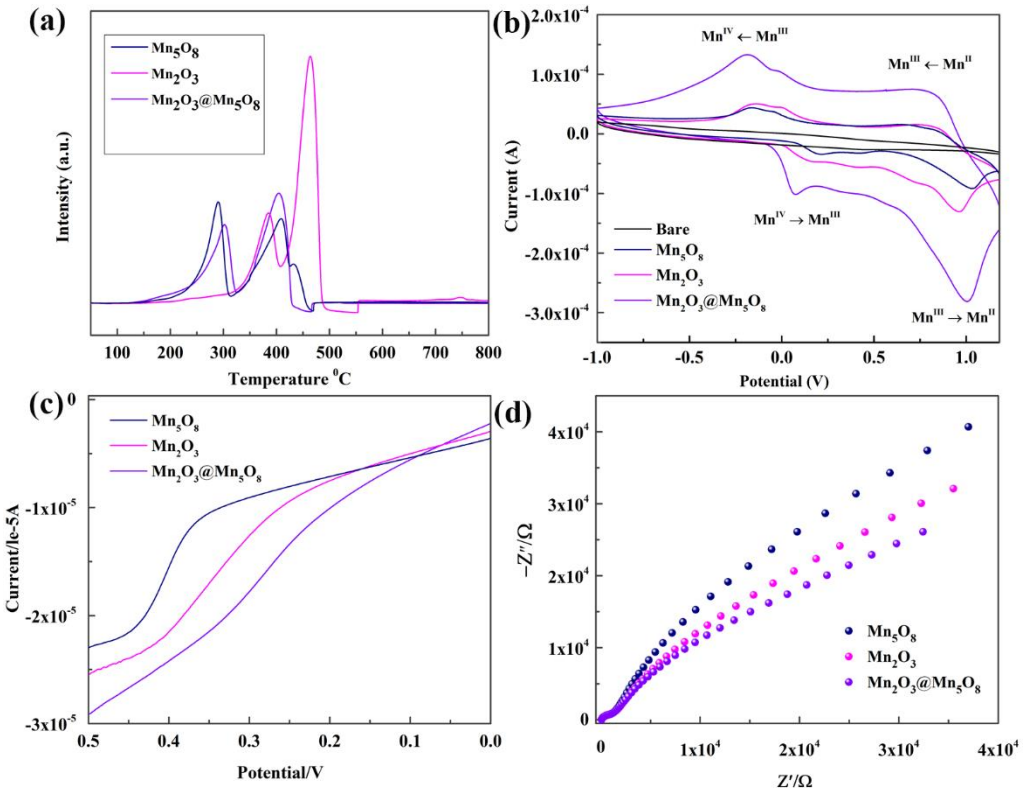

826

827 **Fig. 6.** (a) H_2-TPR profiles of the $Mn_2O_3@Mn_5O_8$, Mn_2O_3, and Mn_5O_8 catalysts, **(b)** CVs obtained

828 on $Mn_2O_3@Mn_5O_8$, Mn_2O_3, and Mn_5O_8 as electrodes in a mixed solution of Na_2SO_4 (0.1 M) and

829 S(IV) (0.7 mM). Scan rate= 100 mV s^{-1}, **(c)** LSV curves and **(d)** EIS Nyquist plots.

830

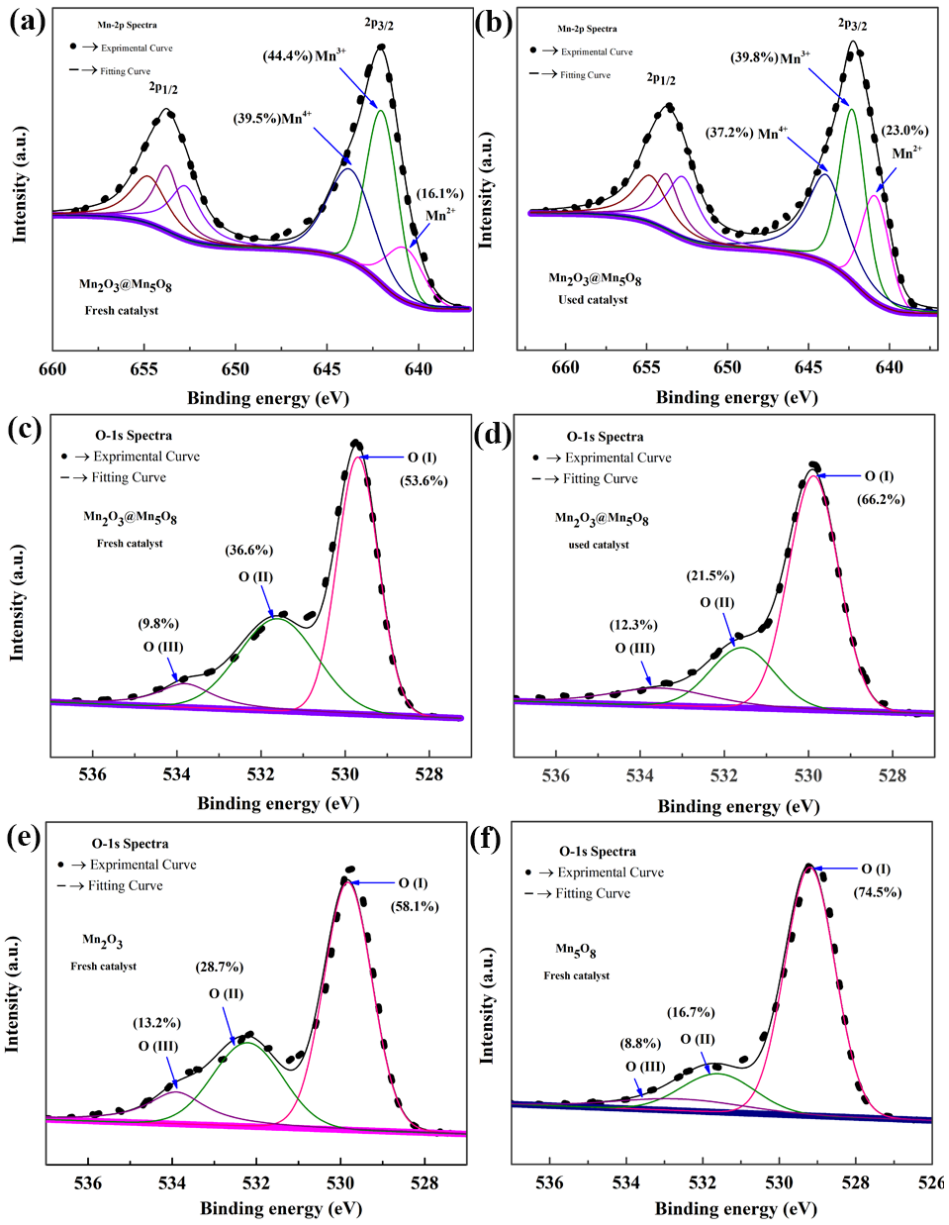

Fig. 7. (a and b) XPS spectra of Mn 2p fresh and used catalyst for the Mn_2O_3@Mn_5O_8. **(c and d)** XPS spectra of O 1s fresh and used catalyst for the Mn_2O_3@Mn_5O_8. XPS spectra of O 1s fresh catalyst for the **(e)** Mn_2O_3 and **(f)** Mn_5O_8**.**

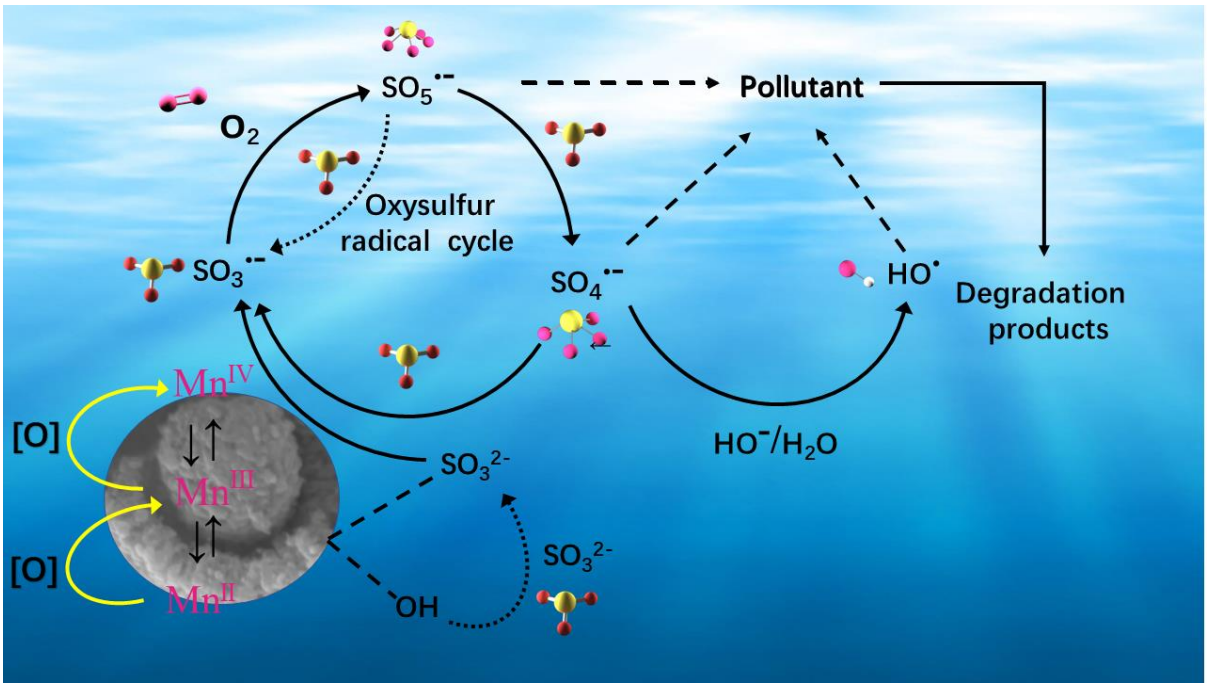

837

838 **Fig. 8.** A possible overall sulfite activation mechanism on Mn_2O_3@Mn_5O_8 catalyst for pollutants
839 degradation.

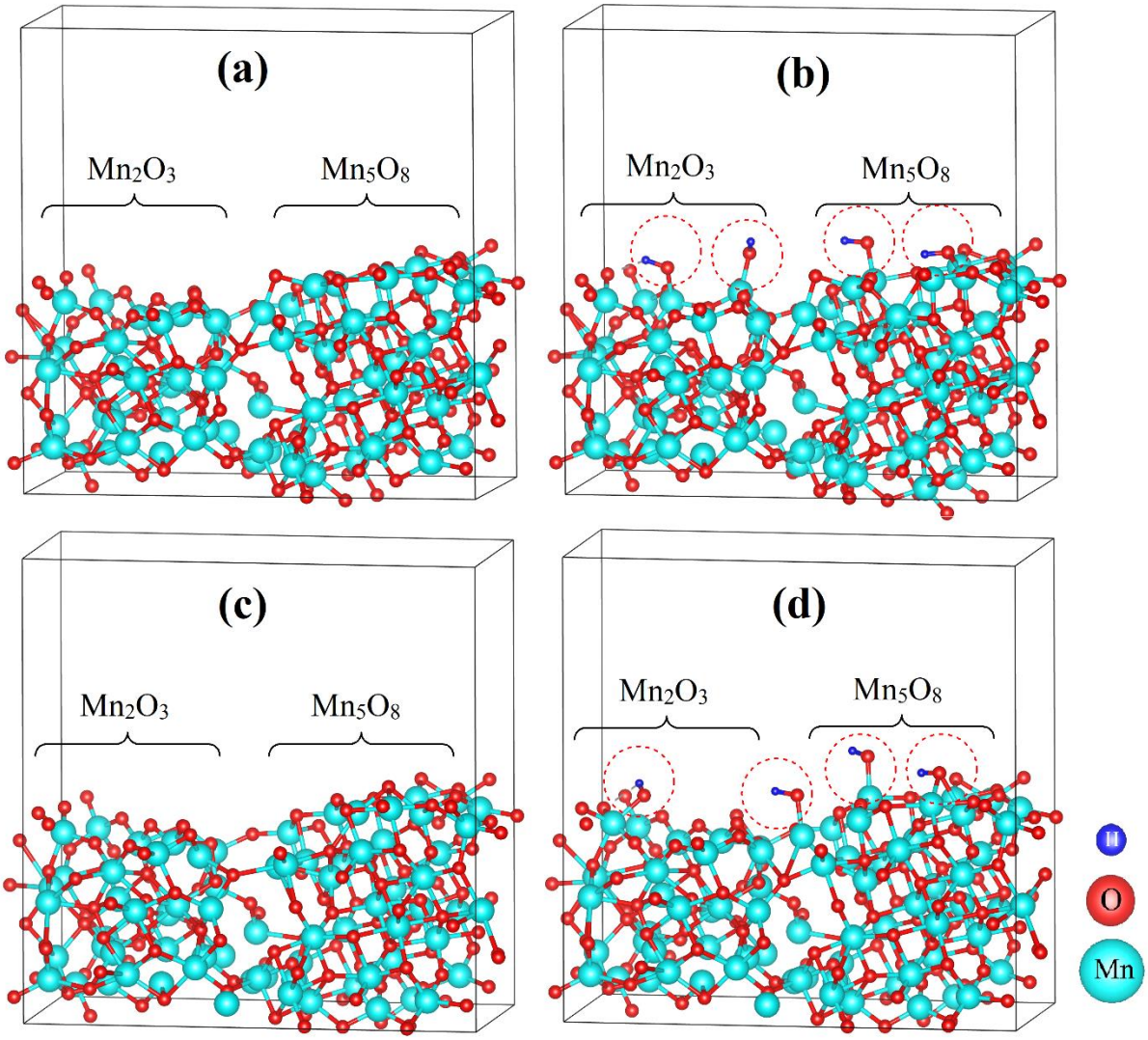

840

841 **Fig. 9.** Optimized relaxed structures of (a) Mn_2O_3@Mn_5O_8(100), (b) Mn_2O_3@Mn_5O_8(100)-OH,
842 (c) Ov-Mn_2O_3@Mn_5O_8(100), and (d) Ov-Mn_2O_3@Mn_5O_8(100)-OH. The adsorbed –OH groups
843 are shown with red broken circles and the Mn_2O_3 and Mn_5O_8 parts are also clearly shown in
844 Figures b and d.

845

846

847

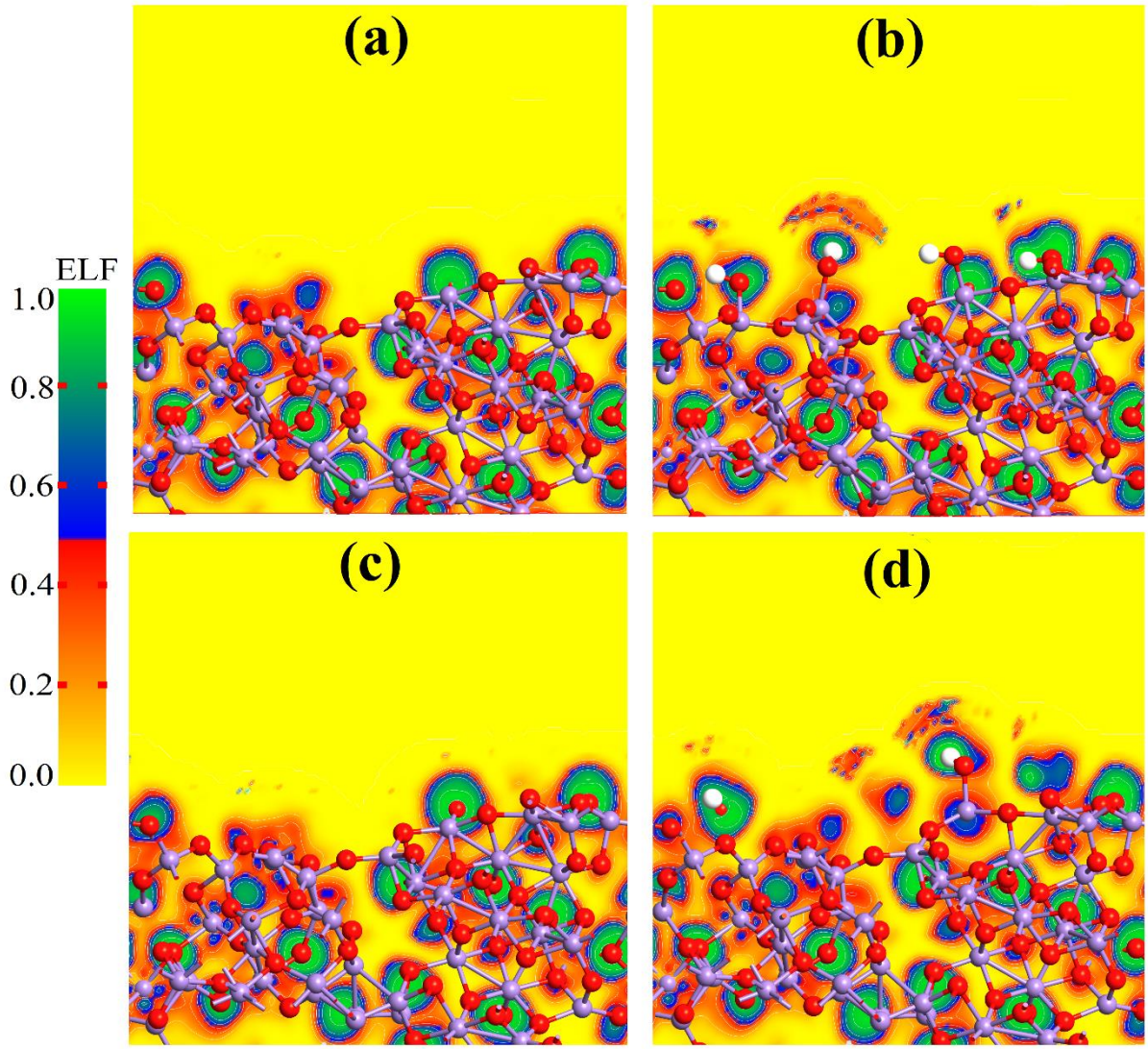

848

849 **Fig. 10**. ELF of (a)Mn_2O_3@Mn_5O_8(100) and (c) its oxygen-deficient, (b, d) form along with –

850 OH interacted species

851

852

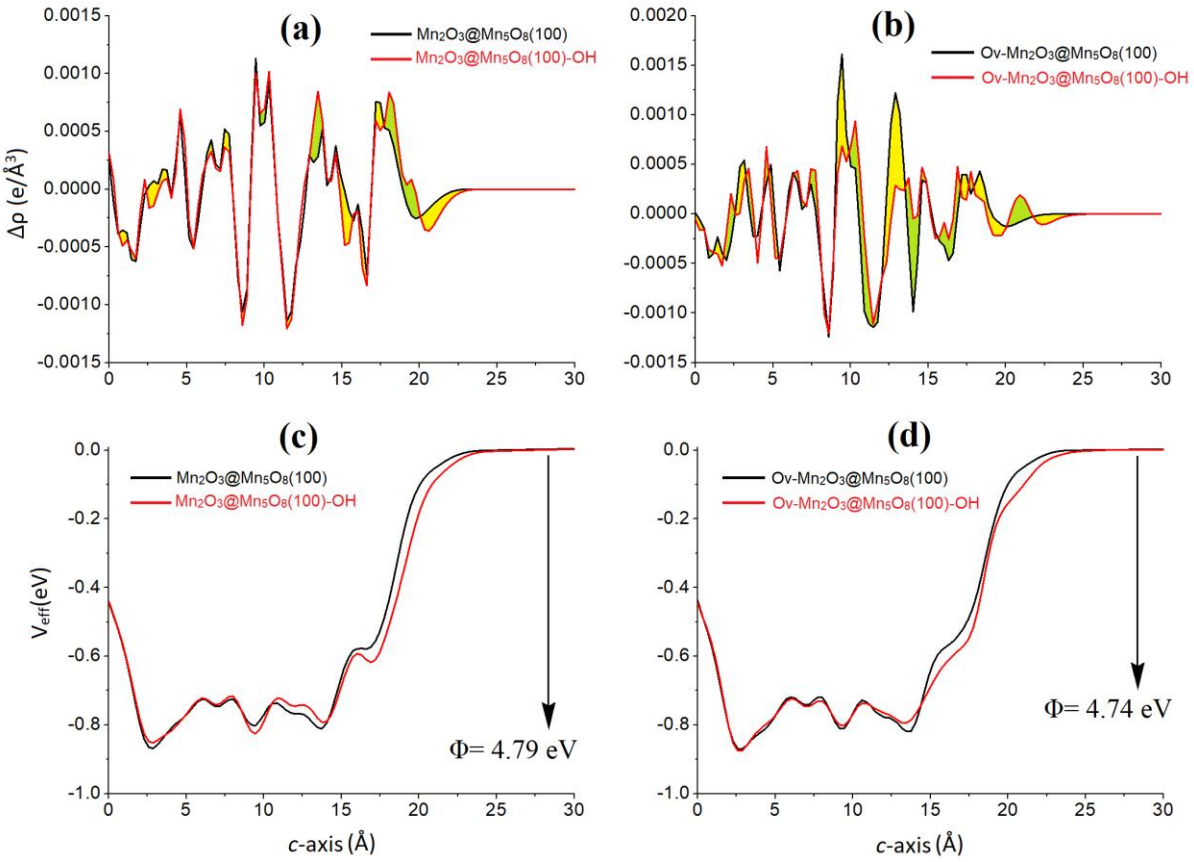

853

854 **Fig. 11.** EDD plot of (a) Mn_2O_3@Mn_5O_8(100) and (b) Ov-Mn_2O_3@Mn_5O_8(100) along with –OH
855 systems, effective potential maps of (c) Mn_2O_3@Mn_5O_8(100) and (d) Ov-Mn_2O_3@Mn_5O_8(100)
856 along with –OH systems. The work function is also shown in the effective potential map plot.

857

858

859

860

861

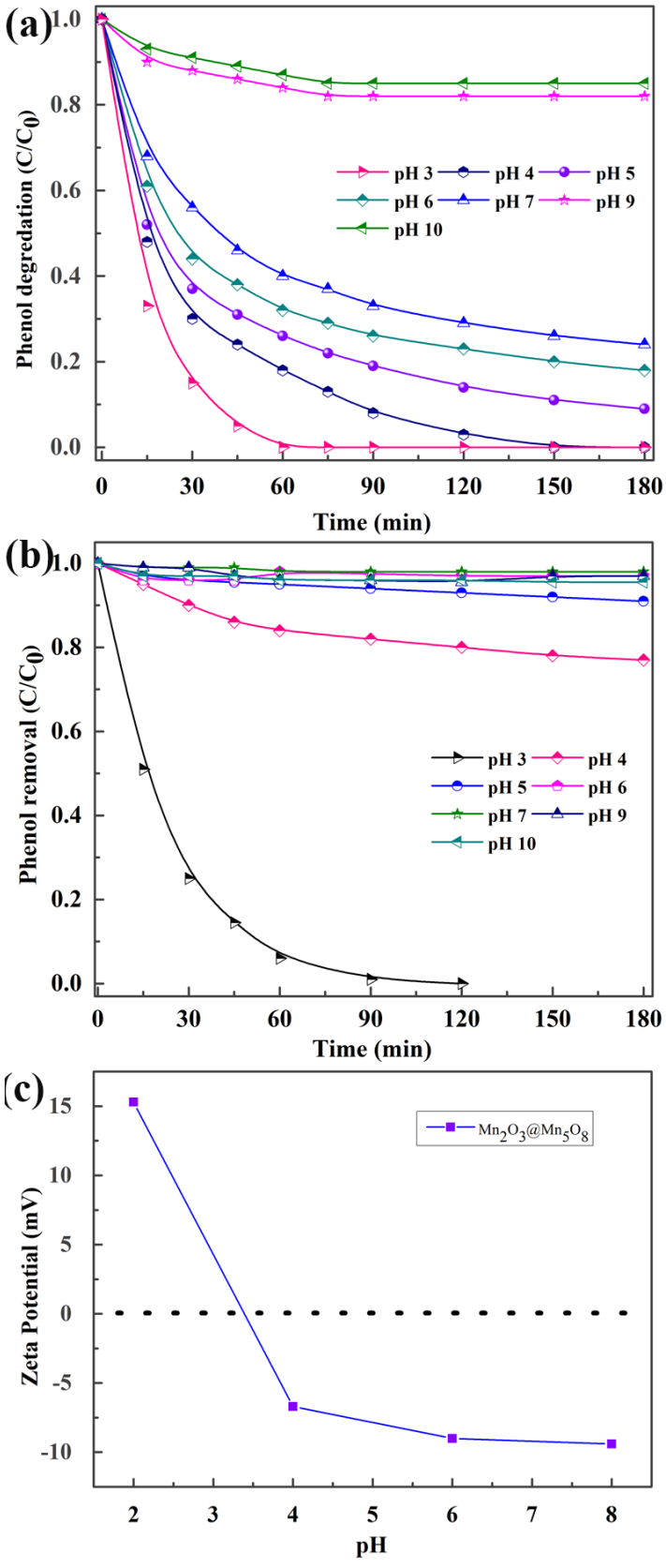

Fig. 12. Effect of initial pH values on **(a)** $Mn_2O_3@Mn_5O_8$/S(IV) system, **(b)** $Mn_2O_3@Mn_5O_8$ alone, **(c)** Zeta Potential (mV) as a function of pH, Reaction conditions: Catalyst 0.2 g/L, sulfite 0.7 mM, phenol 50 μM, and temperature: 30 ˚C.

863

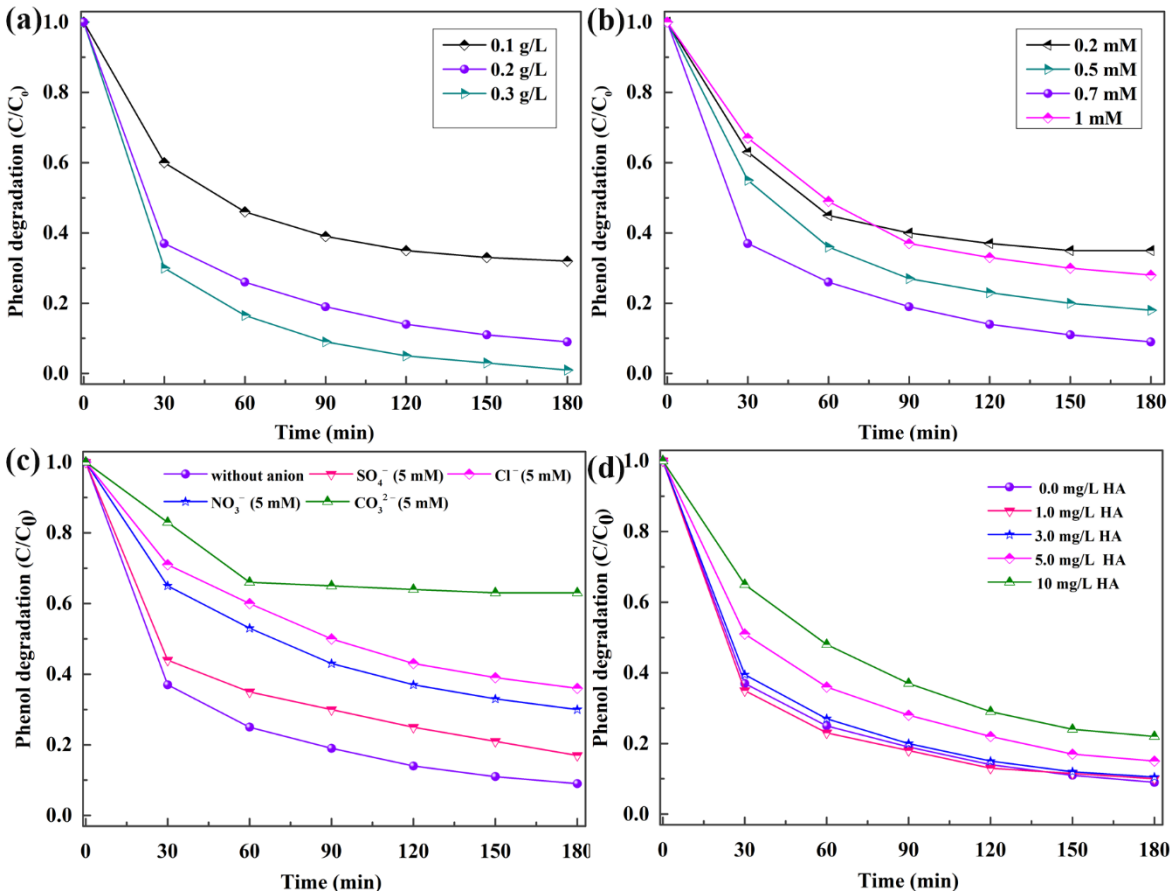

Fig. 13. Effect of **(a)** catalyst dosage, **(b)** sulfite concentration, **(c)** Effect of anion, **(d)** Effect of HA on the degradation of phenol in Mn_2O_3@Mn_5O_8/S(IV) system. Reaction conditions: Catalyst 0.2 g/L, sulfite 0.7 mM, phenol 50 μM, and temperature: 30 ˚C.

874

875

876

877

878

879

880

Conflict of Interest

The authors declare that they have no known competing financial interests or personal relationships that could have appeared to influence the work reported in this paper.